INTERNATIONAL JOURNAL FOR NUMERICAL METHODS IN FLUIDS
Int. J. Numer. Meth. Fluids 2013; **72**:550–582
Published online 21 Nov 2012 in Wiley Online Library (wileyonlinelibrary.com/journal/nmf). DOI: 10.1002/fld.3755

Stability and consistency of nonhydrostatic free-surface models using the semi-implicit θ-method

Sean Vitousek*,† and Oliver B. Fringer

Environmental Fluid Mechanics Laboratory, Stanford University, Stanford, CA, 94305, USA

SUMMARY

The θ-method is a popular semi-implicit finite-difference method for simulating free-surface flows. Problem stiffness, arising because of the presence of both fast and slow timescale processes, is easily handled by the θ-method. In most ocean, coastal, and estuary modeling applications, stiffness is caused by fast surface gravity wave timescales imposed on slower timescales of baroclinic variability. The method is well known to be unconditionally stable for shallow water (hydrostatic) models when $\frac{1}{2} \leqslant \theta \leqslant 1$, where θ is the implicitness parameter. In this paper, we demonstrate that the method is also unconditionally stable for nonhydrostatic models, when $\frac{1}{2} \leqslant \theta \leqslant 1$ for both pressure projection and pressure correction methods. However, the methods result in artificial damping of the barotropic mode. In addition to investigating stability, we also estimate the form of artificial damping induced by both the free surface and nonhydrostatic pressure solution methods. Finally, this analysis may be used to estimate the damping or growth associated with a particular wavenumber and the overall order of accuracy of the discretization. Copyright © 2012 John Wiley & Sons, Ltd.

Received 28 May 2012; Revised 19 October 2012; Accepted 28 October 2012

KEY WORDS: theta-method; stability; accuracy; artificial damping; free surface; nonhydrostatic pressure; ocean modeling

1. INTRODUCTION

The θ-method ("theta"-method) for modeling shallow water flows appeared in [1] and derives its name from the θ or implicitness parameter used in the numerical discretization of the free surface. The benefit of this method is that fast, free-surface gravity waves are discretized semi-implicitly, where $\theta = 0$ is a fully explicit discretization and $\theta = 1$ is fully implicit. When $\theta = 1/2$, the method is the trapezoidal rule or the Crank–Nicolson method [2]. When $1/2 \leqslant \theta \leqslant 1$, the method is unconditionally stable for the representation of free-surface waves [3] and thus allows large timesteps, which otherwise must be quite small for an explicit method in finely spaced or deep water portions of the model domain. Unconditional stability, or A-stability [4], means the numerical solution is stable for any timestep or that the stability region encompasses the entire left half of the complex plane [5]. In fact, the trapezoidal method ($\theta = 0.5$) is quite an optimal method as it represents the A-stable linear multistep method with the smallest truncation error [4].

The θ-method was extended to nonhydrostatic flows in [6]. Several hydrostatic and nonhydrostatic models have adopted this semi-implicit or a purely implicit representation of the free surface including TRIM [1], POP [7], [8], MITgcm [9], ELCOM [10], [11, 12], UnTRIM [13], [14–18], SUNTANS [19], [20], SELFE [21], and FVCOM [22], [23, 24]. There are other models including Delft3D [25], which use the alternating-direction implicit method [26] instead of the θ-method. The

*Correspondence to: Sean Vitousek, Department of Civil and Environmental Engineering, The Jerry Yang and Akiko Yamazaki Environment and Energy Building, 473 Via Ortega, Office M-14, Stanford, CA 94305, USA.

†E-mail: seanv@stanford.edu

predecessors of implicit free-surface models are rigid-lid and mode-split formulations, which are reviewed in [27]. Each approach has numerous advantages and disadvantages. Implicit free-surface models are more common in nonhydrostatic ocean modeling because all terms in the model equations may be treated synoptically without the need for subcycling (although mode-split ocean models such as POM [28] and ROMS [29] have nonhydrostatic solvers in [30] and [31], respectively). Furthermore, the computational cost of solving a two-dimensional elliptic equation for the implicit free surface is small relative to the cost of solving a three-dimensional (3D) elliptic equation for the nonhydrostatic pressure.

In this paper, we investigate the stability of the nonhydrostatic, free-surface θ-method for various pressure projection methods, including the first-order accurate "pressure projection" method [32,33] and the second-order accurate "pressure correction" method [34, 35]. The naming convention of these methods is taken from [36]. In this paper, we show that both methods are unconditionally stable for linear nonhydrostatic free-surface flows. However, both pressure methods can lead to an artificial damping of free-surface waves, which is typically more severe for the first-order accurate pressure projection method. Additionally, we show that the same analysis used to determine the stability of these methods can also be used to estimate the order of accuracy.

The remainder of this paper is divided into five sections. Section 2 presents the governing equations and defining characteristics of nonhydrostatic free-surface flows. Section 3 presents common numerical discretization and solution procedures of the governing equations. Section 4 examines the stability and consistency of the numerical methods. Section 5 presents numerical simulations of nonhydrostatic models and illustrates how stability, numerical damping, and order of accuracy are directly related. Finally, Section 6 presents the conclusions of the methods in this paper.

2. GOVERNING EQUATIONS

The 3D, nonhydrostatic equations of motion under the Boussinesq approximation are given by

$$\frac{\partial \mathbf{u}}{\partial t} + \mathbf{u}\cdot\nabla\mathbf{u} + 2\boldsymbol{\Omega}\times\mathbf{u} = -g\nabla_H\,(h+r) - \nabla q + \nu_H\nabla_H^2\mathbf{u} + \frac{\partial}{\partial z}\left(\nu_V\frac{\partial \mathbf{u}}{\partial z}\right)\,, \tag{1}$$

$$\frac{\partial h}{\partial t} + \nabla_H\cdot\left(\int_{-d}^{h}\mathbf{u}_H\,\mathrm{d}z\right) = 0\,, \tag{2}$$

$$\nabla\cdot\mathbf{u} = 0\,, \tag{3}$$

$$\frac{\partial \rho}{\partial t} + \mathbf{u}\cdot\nabla\rho = K_H\nabla_H^2\rho + \frac{\partial}{\partial z}\left(K_z\frac{\partial \rho}{\partial z}\right)\,, \tag{4}$$

where $\mathbf{u} = [u, v, w]^T$ is the velocity vector ($\mathbf{u}_H = [u, v]^T$ is the vector of horizontal components only), $\boldsymbol{\Omega}$ is the rotation vector, g is the gravity, d is the depth, h is the free-surface height, $r \equiv \frac{1}{\rho_0}\int_z^h \rho'\,\mathrm{d}z$ is the baroclinic pressure head, where ρ_0 is the constant reference density of the fluid and ρ' is the (spatially varying) deviation from the reference density ($\rho' = \rho - \rho_0$), and ν_H, ν_z, K_H, and K_z are the horizontal and vertical viscosities and diffusivities, respectively. The difference between the nonhydrostatic equation set and the hydrostatic equation set is the presence of the nonhydrostatic pressure term involving q on the right-hand side of momentum Equation (1). The normalized nonhydrostatic pressure is given by $q = p_{\mathrm{nh}}/\rho_0$ in the notation following [6], where p_{nh} is the nonhydrostatic or dynamic pressure due to the vertical momentum or acceleration of the fluid. Hydrostatic models do not include the nonhydrostatic pressure term and instead approximate the pressure in the fluid as simply the integrated weight of fluid overhead and ignore the effects of vertical acceleration.

DOI: 10.1002/fld

To understand the behavior of the nonhydrostatic pressure, we examine the nondimensional, inviscid equation set in the absence of rotation and stratification (i.e., assuming a constant density). Governing Equations (1)–(3) are nondimensionalized using

$$x' = \frac{x}{L}, \quad y' = \frac{y}{L}, \quad z' = \frac{z}{D}, \quad t' = \frac{t}{T} = \frac{c_0 t}{L},$$

$$u' = \frac{u}{U}, \quad v' = \frac{v}{U}, \quad w' = \frac{w}{W} = \frac{w}{\epsilon U}, \quad h' = \frac{h}{a}, \quad q' = \frac{q}{U c_0},$$

where $\epsilon = \frac{D}{L}$ is the aspect ratio and $c_0 = \sqrt{gD}$ is the surface gravity wave speed. After ignoring rotation, viscosity, and stratification, omitting the prime notation, and assuming that all quantities are dimensionless, Equations (1)–(3) become

$$\frac{\partial \mathbf{u}_H}{\partial t} + F\mathbf{u} \cdot \nabla \mathbf{u}_H = -\nabla_H q - \nabla_H h, \tag{5}$$

$$\epsilon^2 \frac{\partial w}{\partial t} + \epsilon^2 F \mathbf{u} \cdot \nabla w = -\frac{\partial q}{\partial z}, \tag{6}$$

$$\frac{\partial h}{\partial t} + \nabla_H \cdot \left(\int_{-d}^{Fh} \mathbf{u}_H \, \mathrm{d}z \right) = 0, \tag{7}$$

$$\nabla \cdot \mathbf{u} = 0, \tag{8}$$

where we have chosen the first-order balance between unsteadiness and the hydrostatic pressure gradient, as is typically the case for linear gravity waves, $\delta = F$, where $\delta = \frac{a}{D}$ and $F = \frac{u}{c_0}$.

To determine the nonhydrostatic behavior analytically, we study Equations (5)–(8) in the linear limit, $F \to 0$, in two dimensions (x–z) with a constant depth, so that $d = 1$. The linearized governing equations thus become

$$\frac{\partial u}{\partial t} = -\frac{\partial q}{\partial x} - \frac{\partial h}{\partial x}, \tag{9}$$

$$\epsilon^2 \frac{\partial w}{\partial t} = -\frac{\partial q}{\partial z}, \tag{10}$$

$$\frac{\partial h}{\partial t} = -\frac{\partial}{\partial x} \left(\int_{-1}^{0} u \, \mathrm{d}z \right), \tag{11}$$

$$\frac{\partial u}{\partial x} + \frac{\partial w}{\partial z} = 0. \tag{12}$$

Differentiating Equation (9) with respect to x, differentiating Equation (10) with respect to z and substituting the results into Equation (12) after it has been differentiated with respect to t yield an elliptic equation for the nonhydrostatic pressure q, which is given by

$$\epsilon^2 \frac{\partial^2 q}{\partial x^2} + \frac{\partial^2 q}{\partial z^2} = -\epsilon^2 \frac{\partial^2 h}{\partial x^2}. \tag{13}$$

We will examine the nonhydrostatic behavior of a free-surface seiche by assuming a one-dimensional standing wave for the free surface of the form

$$h = \cos(kx)\cos(\omega t), \tag{14}$$

where k is the horizontal wavenumber or spatial frequency and ω is the temporal frequency or simply frequency. We assume a separable form of the nonhydrostatic pressure, q, where the vertical variation is represented by the structure function $\phi(z)$. Thus, we can write the nonhydrostatic pressure as

$$q(x, z, t) = \phi(z) h(x, t). \tag{15}$$

DOI: 10.1002/fld

Substituting Equations (14) and (15) into the elliptic equation for nonhydrostatic pressure (13) results in an ordinary differential equation for the vertical structure function, which is given by

$$\frac{d^2\phi}{dz^2} - (k\epsilon)^2\phi = (k\epsilon)^2 \,. \tag{16}$$

Equation (16) is subject to the boundary conditions

$$\phi(z=0) = 0, \quad \tfrac{d\phi}{dz}(z=-1) = 0 \,, \tag{17}$$

which arise from the dynamic boundary conditions on the nonhydrostatic pressure

$$q(z=0) = 0, \quad \tfrac{dq}{dz}(z=-1) = 0 \,. \tag{18}$$

The solution of Equation (16) with boundary conditions (17) is given by

$$\phi(z) = \frac{\cosh\left(k\epsilon\,(z+1)\right)}{\cosh\left(k\epsilon\right)} - 1 \,. \tag{19}$$

With this form of the vertical structure function, $\phi(z)$, we can determine solutions to the remaining dependent variables of interest, which are given by

$$q = \phi(z)h = \left(\frac{\cosh\left(k\epsilon\,(z+1)\right)}{\cosh\left(k\epsilon\right)} - 1\right)\cos(kx)\cos(\omega t) \,, \tag{20}$$

$$u = \frac{1}{c}\frac{\cosh\left(k\epsilon\,(z+1)\right)}{\cosh\left(k\epsilon\right)}\sin(kx)\sin(\omega t) \,, \tag{21}$$

$$w = -\frac{1}{c\epsilon}\frac{\sinh\left(k\epsilon\,(z+1)\right)}{\cosh\left(k\epsilon\right)}\cos(kx)\sin(\omega t) \,, \tag{22}$$

where the wave speed, c, is given by $c = \omega/k$ and the form of ω is determined by the dispersion relation, which provides the relationship between the wave frequency and wavenumber. The dispersion relation can be found by deriving a modified wave equation from Equations (9)–(11). Differentiating Equation (11) with respect to t and Equation (9) with respect to x after Equation (15) has been inserted gives

$$\frac{\partial^2 h}{\partial t^2} - (1-\gamma)\frac{\partial^2 h}{\partial x^2} = 0 \,, \tag{23}$$

where γ is defined as the negative of the depth average of the vertical structure function, that is,

$$\gamma \equiv -\int_{-1}^{0} \phi(z)\,\mathrm{d}z \,. \tag{24}$$

We have written Equation (23) with the γ term because it becomes important in our analysis of the stability and consistency of the θ-method in this paper. Evaluating the integral in Equation (24) with the form of the vertical structure function in Equation (19) gives

$$\gamma = 1 - \frac{\tanh(k\epsilon)}{k\epsilon}. \tag{25}$$

Examining the limiting cases for γ, we see that in the hydrostatic limit, $k\epsilon \to 0$, and thus, $\gamma \to 0$. In the nonhydrostatic limit, $k\epsilon \to \infty$, and $\gamma \to 1$. Thus, γ, which we refer to as the normalized nonhydrostasy parameter, ranges from 0 to 1 depending on the degree of nonhydrostasy. The coefficient, $1-\gamma$, in front of the second spatial derivative in Equation (23) is the square of the modified wave speed, that is,

$$c^2 = \frac{\omega^2}{k^2} = 1 - \gamma = \frac{\tanh(k\epsilon)}{k\epsilon} \,.$$

DOI: 10.1002/fld

Thus, the nonhydrostatic dispersion relation for Equations (9)–(12) is given by

$$\omega^2 = \frac{k}{\epsilon}\tanh(k\epsilon)\,, \tag{26}$$

which is the well-known (nondimensional) dispersion relation for free-surface gravity waves [37]. This analysis implies that the magnitude of the nonhydrostatic effects is given by the parameter $k\epsilon$. Waves that vary slowly in the horizontal on thin aspect ratio domains result in small values of $k\epsilon$ and thus flows that are nearly hydrostatic. Rapidly varying waves on deep aspect ratio domains result in large values of $k\epsilon$ and significant nonhydrostatic effects.

This analysis implies that the effect of the nonhydrostatic pressure, through the integral of the vertical structure function, is to decrease the speed of the waves. The main characteristic of nonhydrostatic processes, in contrast to hydrostatic processes, is variation with depth. We have shown that the depth variability is given by the vertical structure function $\phi(z)$. This function and its integrated counterpart, γ, play important roles in many physical aspects of nonhydrostatic processes as well as the analytical and numerical solution of the nonhydrostatic equation set.

3. NUMERICAL APPROXIMATION

The governing Equations, (9)–(12), discretized in two dimensions (x–z) using the θ-method on a staggered grid, where the velocity points are defined at the cell faces and the pressure and free surface are defined at the cell centers, are given by

$$u^{n+1}_{j+1/2,k} = \tilde{F}u^n_{j+1/2,k} - \theta\Delta t\frac{h^{n+1}_{j+1} - h^{n+1}_j}{\Delta x} - (1-\theta)\Delta t\frac{h^n_{j+1} - h^n_j}{\Delta x} - \Delta t\frac{q^{n+1/2}_{j+1,k} - q^{n+1/2}_{j,k}}{\Delta x}\,, \tag{27}$$

$$w^{n+1}_{j,k+1/2} = \tilde{F}w^n_{j,k+1/2} - \Delta t\frac{1}{\epsilon^2}\frac{q^{n+1/2}_{j,k+1} - q^{n+1/2}_{j,k}}{\Delta z}\,, \tag{28}$$

$$h^{n+1}_j = h^n_j - \Delta t\frac{\Delta z}{\Delta x}\sum_{k=1}^{N_z}\left[\theta\left(u^{n+1}_{j+1/2,k} - u^{n+1}_{j-1/2,k}\right) + (1-\theta)\left(u^n_{j+1/2,k} - u^n_{j-1/2,k}\right)\right]\,, \tag{29}$$

$$\frac{u^{n+1}_{j+1/2,k} - u^{n+1}_{j-1/2,k}}{\Delta x} + \frac{w^{n+1}_{j,k+1/2} - w^{n+1}_{j,k-1/2}}{\Delta z} = 0\,, \tag{30}$$

where j is the horizontal grid point index and k is the vertical grid point index. The "theta" method derives its name from the θ or implicitness parameter. The method becomes fully implicit in the discretization of the free surface when $\theta = 1$, fully explicit when $\theta = 0$, and semi-implicit when $0 < \theta < 1$. In Equation (29), we have written the integral discretely as $\int_{-1}^{0} u\,\mathrm{d}z = \Delta z\sum_{k=1}^{N_z} u$, where N_z is the number of (uniformly spaced) grid points in the vertical direction. Here, we have ignored the free-surface nonlinearity. To include this, we must write the integral discretely as $\int_{-1}^{Fh} u\,\mathrm{d}z = \sum_{k=1}^{N_z}\Delta z_k u$, where the grid spacing in the top layer is a function of the free-surface height [6]. We do not consider the free-surface nonlinearity because we are primarily interested in understanding the numerical method for solving the linear nonhydrostatic equations. The numerical method to include the free-surface nonlinearity is fairly standard as in [6]. We do, however, include the advective nonlinearity in our analysis (through the parameter $\tilde{F}$) to study the numerical effects of the choice of advection scheme that can vary significantly.

In Equations (27) and (28), $\tilde{F}$ is a finite-difference operator, after [6], that includes the advection and viscous terms. For example, if the nondimensional advection of momentum and viscous terms

DOI: 10.1002/fld

where included and discretized explicitly, then the operator, presented here in quasi-linear form, is given by

$$\tilde{F} = \left[1 - \Delta t F u_0 \frac{\tilde{\delta}()}{\tilde{\delta}x} - \Delta t F w_0 \frac{\tilde{\delta}()}{\tilde{\delta}z} + \Delta t F \frac{1}{\mathrm{Re}_x} \frac{\tilde{\delta}^2()}{\tilde{\delta}x^2} + \Delta t F \frac{1}{\epsilon^2} \frac{1}{\mathrm{Re}_z} \frac{\tilde{\delta}^2()}{\tilde{\delta}z^2}\right](), \tag{31}$$

where u_0 and w_0 are the effective horizontal and vertical velocities and $\mathrm{Re}_x = \frac{UL}{\nu_H}$ and $\mathrm{Re}_z = \frac{UL}{\nu_z}$ are the horizontal and vertical Reynolds numbers, respectively. We note that the partial derivatives in Equation (31) with the $\tilde{\delta}$ symbol represent discrete partial derivatives. In Equation (31), the viscous terms are discretized explicitly, which creates a timestep restriction based on the viscous Courant numbers $C_{\nu_H} = \frac{2\nu_H \Delta t}{\Delta x^2}$, $C_{\nu_z} = \frac{2\nu_z \Delta t}{\Delta z^2}$. Thus, it is often preferable to discretize the viscous terms implicitly, particularly in the vertical direction as in [1,6] to eliminate the timestep restriction associated with vertical diffusion. In the analysis in this paper, we only consider the inviscid case and use the operator $\tilde{F}$ to study the influence of the momentum advection scheme.

In the family of pressure projection or fractional step methods, provisional horizontal velocities, u^* and w^*, are computed using a reduced number of terms in the momentum equation given by

$$u^*_{j+1/2,k} = \tilde{F} u^n_{j+1/2,k} - \theta \Delta t \frac{h^{n+1}_{j+1} - h^{n+1}_j}{\Delta x} - (1-\theta)\Delta t \frac{h^n_{j+1} - h^n_j}{\Delta x} - \alpha \Delta t \frac{q^{n-1/2}_{j+1,k} - q^{n-1/2}_{j,k}}{\Delta x}, \tag{32}$$

$$w^*_{j,k+1/2} = \tilde{F} w^n_{j,k+1/2} - \alpha \frac{\Delta t}{\epsilon^2} \frac{q^{n-1/2}_{j,k+1} - q^{n-1/2}_{j,k}}{\Delta z}. \tag{33}$$

In Equations (32) and (33), the parameter α designates use of the pressure projection method ($\alpha = 0$) or the pressure correction method ($\alpha = 1$).

Later, the final velocities can be calculated with the addition of the nonhydrostatic terms

$$u^{n+1}_{j+1/2,k} = u^*_{j+1/2,k} - \Delta t \frac{(q_c)^{n+1/2}_{j+1,k} - (q_c)^{n+1/2}_{j,k}}{\Delta x}, \tag{34}$$

$$w^{n+1}_{j,k+1/2} = w^*_{j,k+1/2} - \frac{\Delta t}{\epsilon^2} \frac{(q_c)^{n+1/2}_{j,k+1} - (q_c)^{n+1/2}_{j,k}}{\Delta z}, \tag{35}$$

where q_c, the nonhydrostatic correction pressure, enforces the divergence-free constraint on the velocity field. Substituting final velocities (34) and (35), provisional velocities (32) and (33), into discrete free-surface Equation (29) gives

$$\begin{aligned} h^{n+1}_j - \frac{\theta^2 \Delta t^2}{\Delta x^2}\left(h^{n+1}_{j+1} - 2h^{n+1}_j + h^{n+1}_{j-1}\right) &= h^n_j + \frac{\theta(1-\theta)\Delta t^2}{\Delta x^2}\left(h^n_{j+1} - 2h^n_j + h^n_{j-1}\right) \\ &\quad - \frac{\Delta t \Delta z}{\Delta x} \sum_{k=1}^{N_z} \left(\left(1 - \theta(1-\tilde{F})\right)\left(u^n_{j+1/2,k} - u^n_{j-1/2,k}\right)\right) \\ &\quad + \alpha\theta\Delta t^2 \frac{\Delta z}{\Delta x^2} \sum_{k=1}^{N_z} \left(q^{n-1/2}_{j+1,k} - 2q^{n-1/2}_{j,k} + q^{n-1/2}_{j-1,k}\right) \\ &\quad + \beta\theta\Delta t^2 \frac{\Delta z}{\Delta x^2} \sum_{k=1}^{N_z} \left((q_c)^{n+1/2}_{j+1,k} - 2(q_c)^{n+1/2}_{j,k} + (q_c)^{n+1/2}_{j-1,k}\right), \end{aligned} \tag{36}$$

which is a tridiagonal equation (a pentadiagonal equation in 3D) for the free surface at the new time step, h^{n+1}. Although both projection and correction are second-order accurate in time when $\beta = 1$, Equation (36) is typically solved without the last term ($\beta = 0$) to reduce computational overhead associated with iterating to solve the nonhydrostatic pressure Poisson equation. When $\beta = 0$,

DOI: 10.1002/fld

the projection is first-order accurate in time, and the correction is second-order accurate in time [38]. Without the iterative procedure ($\beta = 0$), the nonlinear free-surface equation can be inconsistent with the divergence-free velocity field obtained after the pressure projection step. If this final divergence-free velocity field is used in passive scalar transport, then the discrete maximum principle can be violated because of lack of the consistency with continuity property as defined in [39]. Thus to avoid inconsistency with continuity, either an iterative procedure ($\beta = 1$) or use of the hydrostatic (provisional) velocities in the scalar transport equation is required.

A discrete Poisson equation can be obtained by substituting the expressions for the final divergence-free velocities, (34) and (35), into discrete incompressibility Equation (30), resulting in

$$\epsilon^2 \frac{(q_c)^{n+1/2}_{j+1,k} - 2(q_c)^{n+1/2}_{j,k} + (q_c)^{n+1/2}_{j-1,k}}{\Delta x^2} + \frac{(q_c)^{n+1/2}_{j,k+1} - 2(q_c)^{n+1/2}_{j,k} + (q_c)^{n+1/2}_{j,k-1}}{\Delta z^2} = \frac{\epsilon^2}{\Delta t}\left(\frac{u^*_{j+1/2,k} - u^*_{j-1/2,k}}{\Delta x} + \frac{w^*_{j,k+1/2} - w^*_{j,k-1/2}}{\Delta z}\right). \tag{37}$$

Substituting the provisional velocities, (32) and (33), into Equation (37) provides a discrete representation of Poisson Equation (13), which is given by

$$\begin{aligned} &\epsilon^2 \frac{(q_c)^{n+1/2}_{j+1,k} - 2(q_c)^{n+1/2}_{j,k} + (q_c)^{n+1/2}_{j-1,k}}{\Delta x^2} + \frac{(q_c)^{n+1/2}_{j,k+1} - 2(q_c)^{n+1/2}_{j,k} + (q_c)^{n+1/2}_{j,k-1}}{\Delta z^2} \\ &\quad + \alpha\left(\epsilon^2 \frac{q^{n-1/2}_{j+1,k} - 2q^{n-1/2}_{j,k} + q^{n-1/2}_{j-1,k}}{\Delta x^2} + \frac{q^{n-1/2}_{j,k+1} - 2q^{n-1/2}_{j,k} + q^{n-1/2}_{j,k-1}}{\Delta z^2}\right) \\ &= \left(\epsilon^2 \frac{q^{n+1/2}_{j+1,k} - 2q^{n+1/2}_{j,k} + q^{n+1/2}_{j-1,k}}{\Delta x^2} + \frac{q^{n+1/2}_{j,k+1} - 2q^{n+1/2}_{j,k} + q^{n+1/2}_{j,k-1}}{\Delta z^2}\right) \\ &= -\epsilon^2\left(\theta \frac{h^{n+1}_{j+1} - 2h^{n+1}_j + h^{n+1}_{j-1}}{\Delta x^2} + (1-\theta)\frac{h^n_{j+1} - 2h^n_j + h^n_{j-1}}{\Delta x^2}\right), \end{aligned} \tag{38}$$

where the normalized nonhydrostatic pressure at time step $n + 1/2$ is given as $q^{n+1/2} = q_c^{n+1/2} + \alpha q^{n-1/2}$. We note that the nonlinear advection of momentum terms does not appear in Equation (38) because the quasi-linear approximation to $\tilde{F}$ operates on the discrete divergence of the velocity field at time step n, which is identically zero. This is not the case in fully nonlinear models or on collocated (nonstaggered) grids as the divergence-free condition is not satisfied discretely to machine-zero. In such cases, Equation (37) must be used or the nonlinear terms must be included in the right-hand side of Equation (38).

The numerical solution procedure of the method outlined earlier is as follows:

1. Solve implicit Equation (36) for the free surface at time step $n + 1$.
2. Calculate the provisional velocities, (32) and (33).
3. Solve the elliptic equation for the nonhydrostatic correction pressure using Equation (37) or (38).
4. If iteration is required ($\beta = 1$), return to step 1 and repeat until convergence is reached.
5. Calculate the final divergence-free velocities using (34) and (35). Alternatively, the final horizontal velocity can be computed using (34), and the vertical velocity can be computed by integrating divergence-free condition (30) from the bottom boundary upward as in [19].

We examine the convergence properties of the iterative ($\beta = 1$) nonhydrostatic method in detail in Appendix D.

DOI: 10.1002/fld

4. PROPERTIES OF THE METHOD

4.1. Stability

To derive the stability properties of the method, we adopt the following vector notation:

$$\mathbf{u} = \left[u_{j,1}, u_{j,2}, \ldots, u_{j,N_z}\right]^T ,$$
$$\mathbf{q} = \left[q_{j,1}, q_{j,2}, \ldots, q_{j,N_z}\right]^T ,$$

where each vector represents the variables of a column of grid points. In vector form, Equations (27) and (36) become

$$\mathbf{u}^{n+1} = \tilde{F}\mathbf{u}^n - \theta\Delta t \mathbf{e} G_x h^{n+1} - (1-\theta)\,\Delta t \mathbf{e} G_x h^n - \Delta t G_x \mathbf{q}^{n+1/2} , \tag{39}$$

$$\begin{aligned}\left(1-\theta^2\Delta t^2 L_{xx}\right) h^{n+1} = &-\Delta t \Delta z \mathbf{e}^T D_x (1-\theta(1-\tilde{F}))\mathbf{u}^n + \left(1+\theta\,(1-\theta)\,\Delta t^2 L_{xx}\right) h^n , \\ &+ \alpha\theta\Delta t^2 \Delta z \mathbf{e}^T L_{xx}\mathbf{q}^{n-1/2} + \beta\theta\Delta t^2 \Delta z \mathbf{e}^T L_{xx}\mathbf{q}_c^{n+1/2} ,\end{aligned} \tag{40}$$

where $\mathbf{e} = [1, 1, \ldots, 1]^T$ with N_z entries. G_x, D_x, and L_{xx} represent the discrete gradient, divergence, and Laplacian operators, respectively, which are given by

$$G_x = \frac{()_{j+1,k} - ()_{j,k}}{\Delta x} ,$$
$$D_x = \frac{()_{j+1/2,k} - ()_{j-1/2,k}}{\Delta x} ,$$

and $L_{xx} = D_x G_x$. Defining the depth-averaged velocity as

$$U \equiv \Delta z \mathbf{e}^T \mathbf{u} ,$$

and after multiplying momentum Equation (39) by $\Delta z \mathbf{e}^T$, governing Equations (39) and (40) become

$$U^{n+1} = \tilde{F}U^n - \theta\Delta t G_x h^{n+1} - (1-\theta)\,\Delta t G_x h^n - \Delta t \Delta z \mathbf{e}^T G_x \mathbf{q}^{n+1/2} , \tag{41}$$

$$\begin{aligned}\left(1-\theta^2\Delta t^2 L_{xx}\right) h^{n+1} = &-\Delta t D_x (1-\theta(1-\tilde{F}))U^n + \left(1+\theta\,(1-\theta)\,\Delta t^2 L_{xx}\right) h^n \\ &+ \alpha\theta\Delta t^2 \Delta z \mathbf{e}^T L_{xx}\mathbf{q}^{n-1/2} + \beta\theta\Delta t^2 \Delta z \mathbf{e}^T L_{xx}\mathbf{q}_c^{n+1/2} ,\end{aligned} \tag{42}$$

where we note that $\Delta z \mathbf{e}^T \mathbf{e} = \Delta z N_z = 1$. In the following analysis, we investigate stability of the free surface and depth-averaged flow. Stability of the full (nondepth averaged) flow is demonstrated in Appendix B.

By assuming periodic solutions in space of the form

$$U = U_0 \exp(ikx_j + ik\Delta x/2) ,$$
$$h = h_0 \exp(ikx_j) ,$$
$$q = q_0 \exp(ikx_j) ,$$

the discrete gradient, divergence, and Laplacian operators can be written as

$$D_x = ik' ,$$
$$G_x = ik' ,$$
$$L_{xx} = -k'^2 ,$$

DOI: 10.1002/fld

where k' is the modified wave number, $k' = 2\sin(k\Delta x/2)/\Delta x$, and $k'^2 = 2[1-\cos(k\Delta x)]/\Delta x^2$. Substitution into discrete Equations (41) and (42) gives

$$U^{n+1} = \tilde{F}U^n - i\theta k'\Delta t h^{n+1} - i\,(1-\theta)\,k'\Delta t h^n - ik'\Delta t\Delta z\mathbf{e}^T\mathbf{q}^{n+1/2}\,, \tag{43}$$

$$\begin{aligned}\left(1+\theta^2(k'\Delta t)^2\right)h^{n+1} = &-ik'\Delta t(1-\theta(1-\tilde{F}))U^n + \left(1-\theta\,(1-\theta)\,(k'\Delta t)^2\right)h^n \\ &-\alpha\theta(k'\Delta t)^2\Delta z\mathbf{e}^T\mathbf{q}^{n-1/2} - \beta\theta(k'\Delta t)^2\Delta z\mathbf{e}^T\mathbf{q}_c^{n+1/2}\,.\end{aligned} \tag{44}$$

After assuming a periodic solution for $\mathbf{q}$, the vector form of pressure Poisson Equation (38) is given by

$$-(k'\epsilon)^2\mathbf{q}^{n+1/2} - \mathbf{M}\mathbf{q}^{n+1/2} = (k'\epsilon)^2\mathbf{e}\left[\theta h^{n+1} + (1-\theta)h^n\right]\,, \tag{45}$$

where, after imposing a Dirichlet boundary condition to satisfy $q = 0$ at $z = 0$ and a Neumann boundary condition to satisfy $\frac{\partial q}{\partial z} = 0$ at $z = -1$, the tridiagonal matrix $\mathbf{M}$ is given by

$$\mathbf{M} = -\frac{1}{\Delta z^2}\begin{bmatrix} -3 & 1 & & & \\ 1 & -2 & 1 & & \\ & \ddots & \ddots & \ddots & \\ & & 1 & -2 & 1 \\ & & & 1 & -1 \end{bmatrix}\,. \tag{46}$$

The discrete solution for the nonhydrostatic pressure is then given by

$$\mathbf{q}^{n+1/2} = -\left[\mathbf{I} + (k'\epsilon)^{-2}\mathbf{M}\right]^{-1}\mathbf{e}\left[\theta h^{n+1} + (1-\theta)h^n\right]\,. \tag{47}$$

Using the short-hand notation, $h^{n+\theta} = \theta h^{n+1} + (1-\theta)h^n$, we can write the discrete solution for nonhydrostatic pressure in (47) as

$$\mathbf{q}^{n+1/2} = -\left[\mathbf{I} + (k'\epsilon)^{-2}\mathbf{M}\right]^{-1}\mathbf{e}h^{n+\theta}\,. \tag{48}$$

Equation (48) is the discrete analogue of the analytical form for the nonhydrostatic pressure, $q = \phi(z)h$, given in Equation (15). The discrete structure function is given by

$$\boldsymbol{\phi}' = -\left[\mathbf{I} + (k'\epsilon)^{-2}\mathbf{M}\right]^{-1}\mathbf{e}\,. \tag{49}$$

The negative depth average of this discrete structure function, which is analogous to the analytical expression for γ (given in Equation (25)), is given by

$$\gamma' = -\Delta z\mathbf{e}^T\boldsymbol{\phi}' = \Delta z\mathbf{e}^T\mathbf{C}\mathbf{e}\,, \tag{50}$$

where $\mathbf{C} = \left[\mathbf{I} + (k'\epsilon)^{-2}\mathbf{M}\right]^{-1}$ and is positive definite. The numerical evaluation γ' has the same limits as the analytical expression for γ, that is, γ' is singly valued and ranges from 0 to 1, as $k\epsilon \to 0$ and $k\epsilon \to \infty$, respectively. The depth-averaged nonhydrostatic pressure, obtained by multiplying $\Delta z\mathbf{e}^T$ by (48), appears in momentum Equation (43) and is thus related to γ' by

$$\Delta z\mathbf{e}^T\mathbf{q}^{n+1/2} = -\Delta z\mathbf{e}^T\mathbf{C}\mathbf{e}h^{n+\theta} = -\gamma' h^{n+\theta}\,. \tag{51}$$

Additionally, similar terms, $\Delta z\mathbf{e}^T\mathbf{q}^{n-1/2}$ and $\Delta z\mathbf{e}^T\mathbf{q}_c$, appear in Equation (44), which have equivalent expressions to Equation (51), which are given by

$$\Delta z\mathbf{e}^T\mathbf{q}^{n-1/2} = -\gamma'\left(\theta h^n + (1-\theta)h^{n-1}\right) = -\gamma' h^{n+\theta-1}\,, \tag{52}$$

$$\begin{aligned}\Delta z\mathbf{e}^T\mathbf{q}_c^{n+1/2} &= \Delta z\mathbf{e}^T\left(\mathbf{q}^{n+1/2} - \alpha\mathbf{q}^{n-1/2}\right) \\ &= \Delta z\mathbf{e}^T\mathbf{q}^{n+1/2} - \alpha\left(\Delta z\mathbf{e}^T\mathbf{q}^{n-1/2}\right) \\ &= -\gamma' h^{n+\theta} + \alpha\gamma' h^{n+\theta-1}\,.\end{aligned} \tag{53}$$

DOI: 10.1002/fld

Substituting Equations (51) into (43) and (52) and (53) into (44) gives (after a great deal of algebra)

$$U^{n+1} + i(1-\gamma')\theta k'\Delta t h^{n+1} = \tilde{F}U^n - i(1-\gamma')(1-\theta)k'\Delta t h^n \,, \tag{54}$$

$$\begin{aligned}\left[1+(1-\beta\gamma')\theta^2(k'\Delta t)^2\right]h^{n+1} = &-ik'\Delta t\left(1-\theta\left(1-\tilde{F}\right)\right)U^n \\ &+\left\{1-\theta\left[(1-\theta)(1-\beta\gamma')-\alpha\gamma'\theta(1-\beta)\right](k'\Delta t)^2\right\}h^n \\ &+\alpha\gamma'(1-\beta)\theta(1-\theta)(k'\Delta t)^2 h^{n-1} \,.\end{aligned} \tag{55}$$

To analyze the stability of the nonhydrostatic method, we consider momentum Equation (54) and free-surface Equation (55) in the following matrix form:

$$\begin{bmatrix} 1 & i(1-\gamma')\theta k'\Delta t & 0 \\ 0 & 1+(1-\beta\gamma')\theta^2(k'\Delta t)^2 & 0 \\ 0 & 0 & 1 \end{bmatrix}\begin{bmatrix} U^{n+1} \\ h^{n+1} \\ h^n \end{bmatrix} =$$

$$\begin{bmatrix} \tilde{F} & -i(1-\gamma')(1-\theta)k'\Delta t & 0 \\ -i\left[1-\theta\left(1-\tilde{F}\right)\right]k'\Delta t & 1-\theta[(1-\theta)(1-\beta\gamma')-\alpha\gamma'\theta(1-\beta)](k'\Delta t)^2 & \alpha\gamma'(1-\beta)\theta(1-\theta)(k'\Delta t)^2 \\ 0 & 1 & 0 \end{bmatrix}\begin{bmatrix} U^n \\ h^n \\ h^{n-1} \end{bmatrix}. \tag{56}$$

This can be written in compact notation as

$$\mathbf{A_1}\mathbf{U}^{n+1} = \mathbf{A_2}\mathbf{U}^n \tag{57}$$

or

$$\mathbf{U}^{n+1} = \mathbf{A}\mathbf{U}^n \,, \tag{58}$$

where $\mathbf{A}$ is the amplification matrix, $\mathbf{A} \equiv \mathbf{A}_1^{-1}\mathbf{A_2}$, $\mathbf{U}^{n+1} = \left[U^{n+1}, h^{n+1}, h^n\right]^T$, and $\mathbf{U}^n = \left[U^n, h^n, h^{n-1}\right]^T$.

Similarly, matrix system (58) can be written as

$$\mathbf{U}^n = \mathbf{A}^n\mathbf{U}^0 \,, \tag{59}$$

which shows that the powers of the matrix (where n is the number of timesteps taken) determine the evolution of the system.

If we write the matrix $\mathbf{A}$ in an eigenvalue/eigenvector decomposition as $\mathbf{A} = \mathbf{X}\mathbf{\Lambda}\mathbf{X}^{-1}$ (provided the matrix has a complete set of eigenvectors), then matrix system (59) becomes

$$\mathbf{U}^n = \mathbf{X}\mathbf{\Lambda}^n\mathbf{X}^{-1}\mathbf{U}^0 \,. \tag{60}$$

System (60) can be decoupled by introducing a new variable $\mathbf{Z} = \mathbf{X}^{-1}\mathbf{U}$ as

$$\mathbf{Z}^n = \mathbf{\Lambda}^n\mathbf{Z}^0 \,. \tag{61}$$

The solution of Equation (61) can be written as

$$Z_p = |\lambda_p|^n Z_0 \exp(in\varphi_p) \,, \tag{62}$$

where p is the component index and $\varphi_p = \tan^{-1}\left(\frac{\text{Imag}(\lambda_p)}{\text{Real}(\lambda_p)}\right)$ is the complex phase. In Equation (62), the magnitude of the eigenvalues controls the amplitude of the solution, and the exponential part controls the phase or oscillation of the solution. Thus, as suggested by Equation (62), to study the stability of the solution, we must examine the magnitude of the eigenvalues of the matrix $\mathbf{A}$. The condition for stability is $\max(|\lambda|) \leq 1$, where λ (without the component subscript) represents all of the eigenvalues of the stability matrix.

The matrix system given by Equation (56) or (59) is very cumbersome to manipulate analytically to determine its eigenvalues and thus its stability properties. On the other hand, it is quite easy to manipulate numerically upon substitution of numerical values for the governing parameters. To

DOI: 10.1002/fld

make this system more tractable, we will examine it in the limit that $k'\Delta t \to \infty$ or simply as the timestep becomes very large. In the other limit, when the timestep becomes very small ($k'\Delta t \to 0$), the matrix system for the linear problem $\left(\tilde{F} = 1.0\right)$ becomes

$$\begin{bmatrix} U^{n+1} \\ h^{n+1} \\ h^n \end{bmatrix} = \begin{bmatrix} 1 & 0 & 0 \\ 0 & 1 & 0 \\ 0 & 1 & 0 \end{bmatrix} \begin{bmatrix} U^n \\ h^n \\ h^{n-1} \end{bmatrix}, \tag{63}$$

which simply states that, as expected, $U^{n+1} = U^n$, $h^{n+1} = h^n$, and trivially, $h^n = h^n$.

In the limit that $k'\Delta t \to \infty$, the linear matrix system $\left(\tilde{F} = 1\right)$ of Equation (56) or (59) becomes

$$\begin{bmatrix} U^{n+1} \\ h^{n+1} \\ h^n \end{bmatrix} = \frac{1}{\theta(1-\beta\gamma')} \begin{bmatrix} \theta(1-\beta\gamma') - (1-\gamma') & -i\alpha\gamma'\theta^2(1-\gamma')(1-\beta)k'\Delta t & -i\alpha\gamma'\theta(1-\theta)(1-\gamma')(1-\beta)k'\Delta t \\ 0 & -(1-\theta)(1-\beta\gamma') + \alpha\gamma'\theta(1-\beta) & \alpha\gamma'(1-\theta)(1-\beta) \\ 0 & \theta(1-\beta\gamma') & 0 \end{bmatrix} \begin{bmatrix} U^n \\ h^n \\ h^{n-1} \end{bmatrix}, \tag{64}$$

which has eigenvalues

$$\lambda_1 = 1 - \frac{1}{\theta}, \tag{65}$$

$$\lambda_2 = 1 - \frac{1}{\theta}\frac{1-\gamma'}{1-\beta\gamma'}, \tag{66}$$

$$\lambda_3 = \alpha\gamma'\frac{1-\beta}{1-\beta\gamma'}. \tag{67}$$

Thus for the system to be stable, $|\lambda| \leqslant 1$, which requires $1/2 \leqslant \theta \leqslant 1$ because γ' ranges from 0 to 1. Therefore, the nonhydrostatic θ-method is unconditionally stable for very large timesteps. Furthermore, if $\theta = 1/2$, then $\lambda_1 = -1$, which implies that the solution will oscillate between positive and negative values of its initial condition without damping. When redimensionalized, the parameter $k'\Delta t$ is proportional to $\omega\Delta t$. In fact, $k'\Delta t = \omega\Delta t$ when the problem is well resolved spatially ($k\Delta x \to 0$). The parameter $\omega\Delta t$ represents the degree to which a wave period is resolved by a timestep Δt. In the typical case, $k'\Delta t \approx \omega\Delta t = 1$ corresponds to approximately $2\pi \approx 6$ timesteps per period of the fastest wave. In the case of fast free-surface gravity waves, $k'\Delta t < 1$ represents the well-resolved case, and $k'\Delta t > 1$ represents the under-resolved case. This under-resolved case, however, is neither uncommon nor avoidable because often the slower time scales of baroclinic variability may be the primary interest. Hence, Equations (65)–(67), which are valid in the limit that $k'\Delta t \to \infty$, provide useful information.

The matrix system given by Equation (59) is much more tractable for an arbitrary value of $k'\Delta t$ when the problem is linear, $\tilde{F} = 1$, and the equations are solved with the pressure projection method ($\alpha = 0$) without iteration ($\beta = 0$). In this case, the amplification matrix $\mathbf{A}$ is a 2×2 matrix and is given by

$$\mathbf{A} = \frac{1}{1 + \theta^2 k'^2 \Delta t^2} \begin{bmatrix} 1 - \theta(1-\theta-\gamma')k'^2\Delta t^2 & -i(1-\gamma')k'\Delta t \\ -ik'\Delta t & 1 - \theta(1-\theta)k'^2\Delta t^2 \end{bmatrix}, \tag{68}$$

where $\mathbf{U} = [U, h]^T$. In this case, the eigenvalues of $\mathbf{A}$ are given by

$$\lambda_{1,2} = 1 - \frac{1}{2}\frac{\theta(2-\gamma')k'^2\Delta t^2 \pm k'\Delta t\sqrt{\theta^2\gamma'^2k'^2\Delta t^2 + 4\gamma' - 4}}{1 + \theta^2 k'^2 \Delta t^2}. \tag{69}$$

In the hydrostatic limit, $\gamma' \to 0$, and the eigenvalues given in Equation (69) become

$$\lambda_{1,2} = \frac{1 - (1-\theta)\theta k'^2\Delta t^2 \pm ik'\Delta t}{1 + \theta^2 k'^2 \Delta t^2}, \tag{70}$$

DOI: 10.1002/fld

which is the equivalent expression for the eigenvalues of the stability matrix derived in [3]. For an arbitrary timestep, the condition for stability requires $|\lambda_{1,2}| \leqslant 1$, where

$$|\lambda_{1,2}| = \sqrt{1 + (1-2\theta)\frac{k'^2\Delta t^2}{1+\theta^2 k'^2 \Delta t^2}} \,. \tag{71}$$

Thus, stability is obtained when $1-2\theta \leqslant 0$ or equivalently $\theta \geqslant \frac{1}{2}$, which is the well-known condition for the free-surface θ-method in [3].

Returning to the nonhydrostatic system, we examine the magnitude of the eigenvalues in Equation (69) when $\gamma' \neq 0$. For small γ', the expression inside the square root of Equation (69) is negative, and the eigenvalues form complex conjugate roots. In this case, the magnitude of the eigenvalues is given by

$$|\lambda_{1,2}| = \sqrt{1 + [(1-2\theta) - (1-\theta)\gamma']\frac{k'^2\Delta t^2}{1+\theta^2 k'^2 \Delta t^2}} \,. \tag{72}$$

The condition $|\lambda_{1,2}| \leqslant 1$ then requires

$$(1-2\theta) - (1-\theta)\gamma' \leqslant 0 \,, \tag{73}$$

which is satisfied provided $1/2 \leqslant \theta \leqslant 1$ and $\gamma' \geqslant 0$, which is indeed the case because the matrix $\mathbf{C}$ in Equation (50) is positive definite. When γ' is large and the expression inside the square root of Equation (69) is positive, the eigenvalues do not necessarily form complex conjugate roots. In this case, the expression for the magnitude of the eigenvalues is more complicated; however, the condition $|\lambda_{1,2}| \leqslant 1$ still holds. These situations are investigated numerically in Section 5.

4.2. Numerical damping and order of accuracy estimates

The stability properties of the numerical method are directly related to the damping (amplitude error) induced by the method and are governed by the eigenvalues of the system. We can also determine the order of accuracy of the numerical method by examining the amplitude and phase error as predicted by the eigenvalues of the stability matrix. If we consider the linear, inviscid equations, then the amplitude of the waves does not decay or grow, and the true eigenvalues of the equations of motion are unity in magnitude, that is, $|\lambda| = 1$. Thus, the amplitude error is given by

$$E_{\text{amp}} = 1 - |\lambda|^n \,. \tag{74}$$

Likewise, the oscillatory part of the true eigenvalues is given by $\exp(i\omega t)$ or $\exp(in\omega\Delta t)$, where ω is given by the dispersion relation, $\omega = \sqrt{\frac{k}{\epsilon}\tanh(k\epsilon)}$ or $\omega = k\sqrt{1-\gamma}$. Thus, the phase error from one timestep is given by $\omega\Delta t - \varphi$. The total phase error after n timesteps is given by

$$E_{\text{phase}} = (\omega\Delta t - \varphi)n \,. \tag{75}$$

Thus, the order of accuracy (in time) can be determined by examining how the amplitude or phase error as determined by the eigenvalues increases with Δt. The overall order of accuracy of the numerical method is given by the lessor of the order of accuracy of the amplitude error or phase error. Numerical experiments comparing the order of accuracy of the numerical model to Equations (74) and (75) are given in Appendix C.

4.3. Numerical dispersion

The problem of numerical dispersion in the context of nonhydrostatic ocean models was studied in [40]. They found that for second-order accurate models, the ratio of numerical to physical dispersion is proportional to the square of the grid lepticity [41], $\tilde{\lambda} \equiv \Delta x/\epsilon$. For completeness, we consider numerical dispersion in the context of staggered grid, finite-difference approximations to nonhydrostatic Equations (9)–(12). We note that the primary goal of this paper is to study numerical stability

DOI: 10.1002/fld

and damping (first-order error). Numerical dispersion (second-order error) is a secondary issue in this paper, both because it is a higher-order effect and because it has been studied extensively in [40].

To illustrate the appearance of numerical dispersion, we analyze the discrete pressure Poisson equation, which following from Equation (13), becomes

$$\epsilon^2 L_{xx}\mathbf{q} + L_{zz}\mathbf{q} = -\mathbf{e}\epsilon^2 L_{xx}h \,. \tag{76}$$

Substituting the modified wavenumber, $L_{xx} = -k'^2$, gives

$$-(k'\epsilon)^2\mathbf{q} + L_{zz}\mathbf{q} = \mathbf{e}(k'\epsilon)^2 h \,. \tag{77}$$

Similar to the analytical approach derived earlier if we assume a separable form of $\mathbf{q} = \boldsymbol{\phi}' h$, this equation reduces to

$$L_{zz}\boldsymbol{\phi}' - (k'\epsilon)^2\boldsymbol{\phi}' = \mathbf{e}(k'\epsilon)^2 \,, \tag{78}$$

which is the discrete analogue of the ordinary differential equation in Equation (16).

If we assume that we can do the vertical integration exactly, then this becomes

$$\boldsymbol{\phi}' = \frac{\cosh(k'\epsilon(z+1))}{\cosh(k'\epsilon)} \,, \tag{79}$$

which is the analogue of Equation (19), and thus, the normalized nonhydrostasy parameter γ' becomes

$$\gamma' = 1 - \frac{\tanh(k'\epsilon)}{k'\epsilon} \,, \tag{80}$$

which is analogous to Equation (25). Thus, the discrete wave equation, following Equation (23), after substituting the modified wavenumber becomes

$$\frac{\partial^2 h}{\partial t^2} + (1-\gamma')k'^2 h = 0 \,, \tag{81}$$

which can be written as

$$\frac{\partial^2 h}{\partial t^2} + \tilde{\sigma}^2(1-\gamma)k^2 h = 0 \,, \tag{82}$$

where

$$\tilde{\sigma}^2 = \frac{k'^2}{k^2}\frac{1-\gamma'}{1-\gamma} \,. \tag{83}$$

Equation (82) is a simple harmonic oscillator equation that has solution $h = h_0 \exp(i\tilde{\omega}t)$, where $\tilde{\omega}^2 = \tilde{\sigma}^2(1-\gamma)k^2$. This equation can be written in terms of the wave speed as follows:

$$\tilde{c}^2 = \tilde{\omega}^2/k^2 = \tilde{\sigma}^2(1-\gamma) \,. \tag{84}$$

Comparing this with the true wave speed $c^2 = 1-\gamma$, we see that the quantity $1-\tilde{\sigma}$ represents the relative error in the wave speed due to the horizontal discretization alone (as the influence of the vertical and time discretization were ignored). The error term can be written as

$$\tilde{\sigma} = \frac{\sin\left(\frac{\tilde{\lambda}}{2}k\epsilon\right)}{\frac{\tilde{\lambda}}{2}k\epsilon}\sqrt{\frac{k\epsilon}{\tanh(k\epsilon)}\frac{\tanh\left(\frac{2}{\tilde{\lambda}}\sin\left(\frac{\tilde{\lambda}}{2}k\epsilon\right)\right)}{\frac{2}{\tilde{\lambda}}\sin\left(\frac{\tilde{\lambda}}{2}k\epsilon\right)}} \,, \tag{85}$$

where

$$\frac{k'}{k} = \frac{\sin\left(\frac{\tilde{\lambda}}{2}k\epsilon\right)}{\frac{\tilde{\lambda}}{2}k\epsilon} \tag{86}$$

DOI: 10.1002/fld

and

$$\frac{1-\gamma'}{1-\gamma} = \frac{\tanh(k'\epsilon)/(k'\epsilon)}{\tanh(k\epsilon)/(k\epsilon)} = \frac{k\epsilon}{\tanh(k\epsilon)} \frac{\tanh\left(\frac{2}{\tilde{\lambda}}\sin\left(\frac{\tilde{\lambda}}{2}k\epsilon\right)\right)}{\frac{2}{\tilde{\lambda}}\sin\left(\frac{\tilde{\lambda}}{2}k\epsilon\right)} . \tag{87}$$

If we ignore the error induced by the solution of the nonhydrostatic Poisson equation and assume that the dispersive error is only due to the misrepresentation of gradient due to the finite-difference approximation, then $\gamma' = \gamma$ and $\tilde{\sigma} = \frac{k'}{k}$. Thus, $\tilde{c} = \pm\tilde{\sigma}\sqrt{1-\gamma}$ becomes

$$\tilde{c} = \pm\sqrt{\left(\frac{\sin\left(\frac{\tilde{\lambda}}{2}k\epsilon\right)}{\frac{\tilde{\lambda}}{2}k\epsilon}\right)^2 \frac{\tanh(k\epsilon)}{k\epsilon}} . \tag{88}$$

Expanding $\sin\left(\frac{\tilde{\lambda}}{2}k\epsilon\right)$ and $\tanh(k\epsilon)$ in Taylor series, then Equation (88), to lowest order, becomes

$$\tilde{c} \approx \pm\sqrt{1-(1+\Gamma)\frac{(k\epsilon)^2}{3}} , \tag{89}$$

where $\Gamma = \frac{\tilde{\lambda}^2}{4}$ is the ratio of numerical to physical dispersion to lowest order. As $\Gamma \to 0$, then Equation (89) approaches the first two terms in the Taylor series expansion of $c = \pm\sqrt{\tanh(k\epsilon)/(k\epsilon)}$. The result that the ratio of numerical to physical dispersion, to lowest order, is proportional to the grid lepticity squared for second-order accurate models was reported in [40], and the present analysis supports that finding. In summary, we have shown the appearance of numerical dispersion arising from the inability to resolve horizontal gradients in the finite-difference approximation. The other sources of error in the model include the vertical discretization and time discretization. However, in general, ensuring that the grid lepticity is small is the primary means of reducing numerical dispersion.

5. NUMERICAL EXPERIMENTS

We present numerical simulations of the hydrostatic and nonhydrostatic θ-methods to verify the theoretical properties derived in the previous section including consistency, stability, and numerical damping. Appendices A and C contain supporting numerical experiments on mode-specific damping and order of accuracy, respectively. Summary of the parameters used in each numerical experiment and corresponding figure is given in Table I. We begin by verifying in Section 5.1 that the hydrostatic and nonhydrostatic simulations behave according to theory.

5.1. Nonhydrostatic dispersion

In Figure 1, we compare the modeled free-surface height and the horizontal and vertical velocity profiles of a free-surface seiche in an enclosed basin to the analytical solutions given in Equations (14), (21), and (22), respectively, at nondimensional time $t = T/8$, where $T = 2L/c$ is the nondimensional period of the seiche. This simulation is performed with parameters given in Table I. Figure 1 displays the nonhydrostatic pressure q and the velocity vectors in panel (B). As seen in this panel, the influence of the free-surface wave decays quickly with depth. The nonhydrostatic pressure, as shown in panel (B), acts to cancel the added hydrostatic pressure due to the free-surface wave (shown in panel (A)). Thus, at depth beyond the influence of the surface wave, the total pressure is given by the still-water hydrostatic pressure. As shown in Figure 1(C) and (D), the modeled velocities agree with the analytical solutions.

Next we compare the speed of modeled free-surface seiche oscillations to the analytical wave speed following the test case given in [19]. The nondimensional nonhydrostatic wave speed given by dispersion relation (26) is $c_{\mathrm{nh}} = \sqrt{\tanh(k\epsilon)/(k\epsilon)} = \sqrt{1-\gamma}$, whereas the hydrostatic wave

DOI: 10.1002/fld

Table I. Numerical experiments.

Figure	N_x	N_z	L	D	Δx	Δz	Δt	C	$k'\Delta t$ (fund.)	ϵ	θ	α	β	$\tilde{F}$	ICs	BCs
1	32	32	1	1	0.03125	0.03125	0.003125	0.1	0.01	1	0.5	1	0	1	$\cos(\pi x/L)$	Closed
2	64	64	1	1	0.015625	0.015625	0.03125	2	0.1	var.	0.5	var.	var.	1	$\cos(\pi x/L)$	Closed
3	var.	NA	NA	NA	var.	NA	NA	NA	NA	NA	NA	NA	NA	1	NA	NA
4	64	64	1	1	0.015625	0.015625	0.15625	10	0.5	0.2	var.	var.	0	1	$\cos(\pi x/L)$	Closed
5	NA	NA	NA	NA	NA	NA	NA	NA	1	NA	var.	var.	var.	1	NA	NA
6	64	64	1	1	0.015625	0.015625	var.	var.	var.	0.5	var.	var.	0	1	$\cos(\pi x/L)$	Closed
7	64	64	1	1	0.015625	0.015625	var.	var.	var.	0.5	var.	var.	0	1	NA	NA
8	NA	NA	NA	NA	NA	NA	NA	NA	var.	NA	var.	var.	0	1+0.2i	NA	NA
9	NA	NA	NA	NA	NA	NA	NA	NA	var.	NA	var.	var.	0	0.8-0.2i	NA	NA
10	128	128	1	1	0.0078125	0.0078125	0.15625	20	1	0.2	0.5	1	0	1	$\sum_j a_j \cos(k_j x/L)$	Closed
11	32	32	1	1	0.03125	0.03125	var.	var.	var.	0.5	var.	var.	var.	1	$\cos(\pi x/L)$	Closed

C, Courant # $= \Delta t/\Delta x$; fund, fundamental; var., variable; NA, not applicable; ICs, initial conditions; BCs, boundary conditions.

DOI: 10.1002/fld

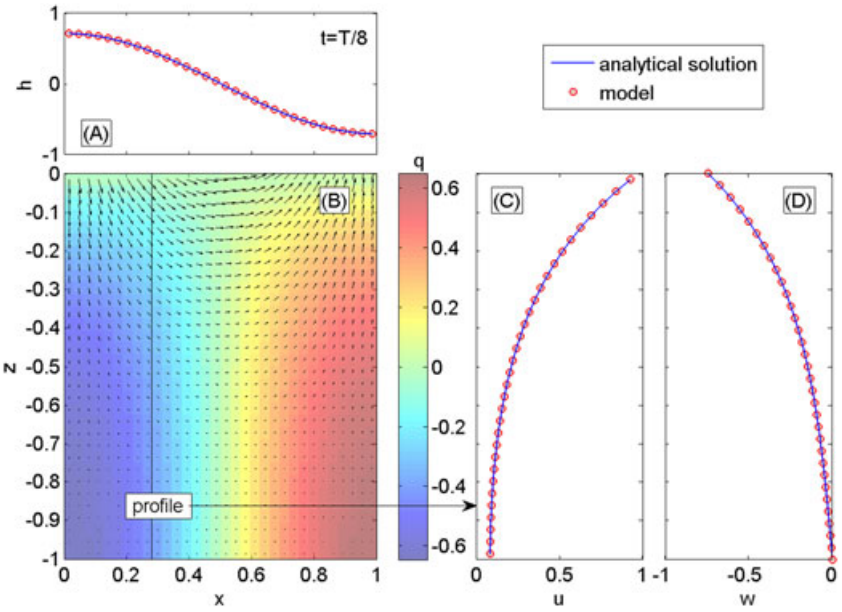

Figure 1. Modeled free-surface height (A), horizontal (C), and vertical velocity profiles (D) of a seiche compared to the analytical solutions, which are given by Equations (14), (21), and (22), respectively, at time $t = T/8$. The nonhydrostatic pressure, q, and velocity vectors are plotted in (B).

speed is $c_{\mathrm{h}} = 1$. As the waves become more nonhydrostatic (as $k\epsilon \to \infty$), the deep water wave speed becomes

$$c_d = \lim_{k\epsilon\to\infty} \sqrt{\frac{\tanh(k\epsilon)}{k\epsilon}} = \frac{1}{\sqrt{k\epsilon}}\,. \tag{90}$$

Thus, the nonhydrostatic and hydrostatic wave speeds normalized by the deep water wave speed become

$$\frac{c_{\mathrm{nh}}}{c_d} = \sqrt{\tanh(k\epsilon)} \tag{91}$$

and

$$\frac{c_{\mathrm{h}}}{c_d} = \sqrt{k\epsilon}\,, \tag{92}$$

respectively. Figure 2 compares these theoretical relationships to the model behavior of oscillating free-surface seiche waves in an enclosed basin. The test case is performed with parameters given in Table I for various degrees of nonhydrostasy $\epsilon = 0.02, 0.05, 0.1, 0.175, 0.27, 0.38, 0.5, 0.65, 0.8, 1.0, 1.2$. These simulations are performed for the projection and correction methods, with and without iteration. The free surface is initialized with $h_0 = \cos(kx)$, and the analytical solution is given by $h = \cos(kx)\cos(\omega t)$, where the wavenumber is given by $k = \pi/L$ and the wave frequency, $\omega = 2\pi/T$, is given by the dispersion relation. The modeled wave speeds are determined by estimating the period of oscillation, T_{modeled}, from the simulation start time to the time of the next maximum in the free surface at $x = 0$ and then calculating the wave speed on the basis of $c_{\mathrm{modeled}} = \omega_{\mathrm{modeled}}/k$. The modeled wave speeds agree with the theoretical relationships for each pressure method as shown in Figure 2, indicating that the model achieves the correct dispersive behavior. When the nonhydrostasy parameter $k\epsilon$ is small, the hydrostatic and nonhydrostatic models are similar. However, when there is an appreciable degree of nonhydrostasy, the hydrostatic model overpredicts the true wave speed. We note that all of the nonhydrostatic methods produce accurate dispersion relations for the fundamental mode, which is why the results in Figure 2 for the nonhydrostatic methods are almost identical.

DOI: 10.1002/fld

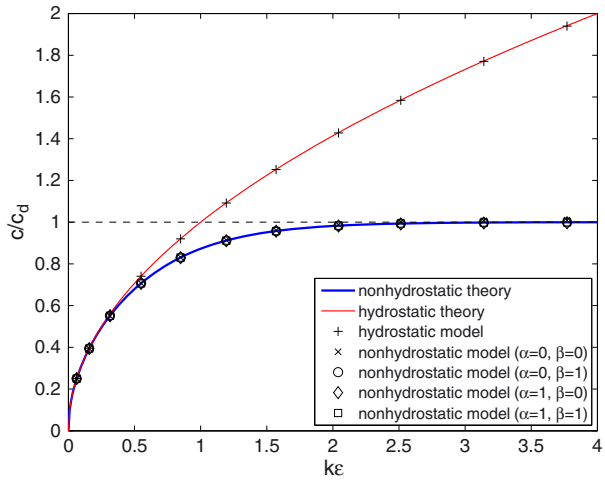

Figure 2. The modeled and theoretical hydrostatic and nonhydrostatic wave speeds normalized by the deep water wave speed as a function of $k\epsilon$. The curves representing the nonhydrostatic and hydrostatic theories are given by Equations (91) and (92), respectively.

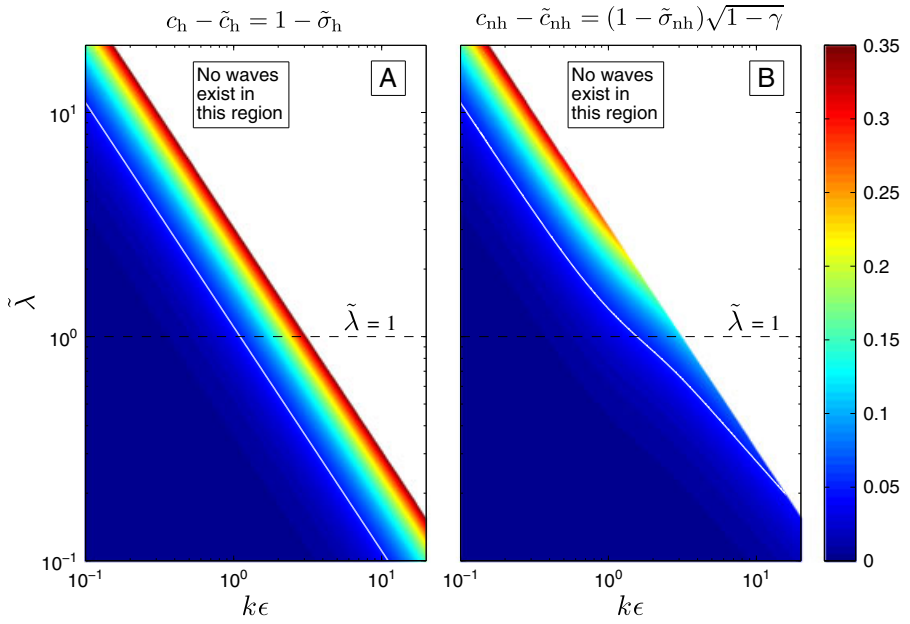

Figure 3. The wave speed error $c - \tilde{c}$ caused by numerical dispersion in hydrostatic (A) and nonhydrostatic models (B) as a function of nonhydrostasy parameter $k\epsilon$ and grid lepticity $\tilde{\lambda} \equiv \Delta x/\epsilon$. The white portion of this figure represents the region in wavenumber space that does not exist on a discrete grid of size Δx, that is, $(k\epsilon)_{\max} = \frac{\pi}{\tilde{\lambda}}$. Dispersive error in the hydrostatic model is persistent at high wavenumbers for all values of Δx or lepticity. On the other hand, the wave speed error in the nonhydrostatic model decreases rapidly when $\tilde{\lambda} < 1$. The white line represents the 5% error contour.

Figure 3 shows the wave speed error caused by numerical dispersion for the hydrostatic and nonhydrostatic models as a function of nonhydrostasy parameter $k\epsilon$ and grid lepticity $\tilde{\lambda} \equiv \Delta x/\epsilon$. Panel (A) of Figure 3 shows the wave speed error for the hydrostatic model, which is given by

$$c_h - \tilde{c}_h = 1 - \tilde{\sigma}_h, \tag{93}$$

DOI: 10.1002/fld

where $\tilde{c}_{\mathrm{h}} = \tilde{\sigma}_{\mathrm{h}}$ is modeled shallow water wave speed and $\tilde{\sigma}_{\mathrm{h}} = \frac{k'}{k}$, which is given by Equation (86). Likewise, Panel (B) shows the wave speed error for the nonhydrostatic model, which is given by

$$c_{\mathrm{nh}} - \tilde{c}_{\mathrm{nh}} = (1 - \tilde{\sigma}_{\mathrm{nh}})\sqrt{1-\gamma}, \tag{94}$$

where $\tilde{c}_{\mathrm{nh}} = \tilde{\sigma}_{\mathrm{nh}}\sqrt{1-\gamma}$ is the modeled nonhydrostatic wave speed and $\tilde{\sigma}_{\mathrm{nh}} = \tilde{\sigma}$, which is given by Equation (85). The white portion of the figure represents the region in wavenumber space that does not exist on a discrete grid of size Δx, that is, $(k\epsilon)_{\max} = \frac{\pi}{\tilde{\lambda}}$. In the hydrostatic case, the dispersion is purely numerical, and thus, dispersive errors exist at high wavenumbers for all values of Δx (or lepticity). However, in the nonhydrostatic model, the wave speed error decreases rapidly when $\tilde{\lambda} < 1$ because the amount of numerical dispersion becomes small relative to the physical dispersion as $\tilde{\lambda}$ decreases.

5.2. *Stability*

As shown in Section 4.2, the cost of stability of the θ-method is artificial damping of the free surface. We showed that artificial damping is related to the magnitude of the eigenvalues of the stability matrix that are functions of the implicitness parameter, θ, and the normalized nonhydrostasy parameter, γ'. Here, we verify with numerical experiments that the envelope of the numerical solution is governed by the eigenvalues.

Figure 4 shows the free-surface height at the left wall ($x = 0$) as a function of time normalized by the wave period. For certain parameters, the amplitude decays as the simulation progresses. As shown in Figure 4, the numerical damping is greatest when $\theta = 1$. However, when $\theta = 0.5$, numerical damping occurs for the projection method without iteration ($\alpha = 0, \beta = 0$). This is due

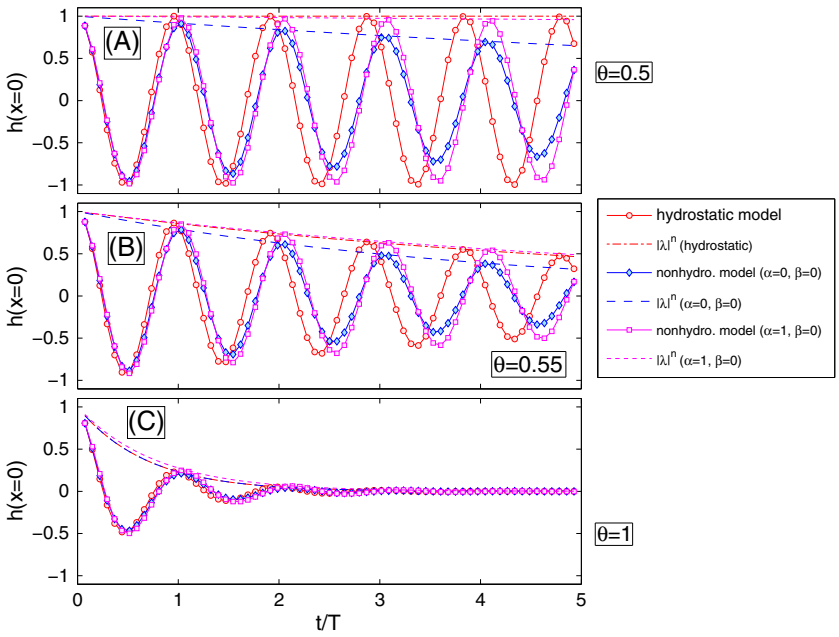

Figure 4. The free-surface height at the left wall ($x = 0$) computed by hydrostatic and nonhydrostatic models as a function of time normalized by the wave period. Panels (A), (B), and (C) show simulations for $\theta = 0.5$, $\theta = 0.55$, and $\theta = 1.0$, respectively. Panel (A) illustrates the numerical damping of the nonhydrostatic model with the pressure projection method ($\alpha = 0$). Note that there is no damping associated with the hydrostatic θ-method when $\theta = 0.5$. The numerical damping in part (A) associated with the pressure correction method ($\alpha = 1$) and iteration methods ($\beta = 1$) is minimal. Panels (B) and (C) show significant damping associated with the free-surface solution procedure when $\theta > 0.5$. This damping is only slightly increased for the nonhydrostatic model with the pressure projection method ($\alpha = 0$). This figure also shows that the amplitude envelope of the numerical solution follows $|\lambda|^n$.

DOI: 10.1002/fld

to the first-order accuracy of the projection method. Use of pressure correction or iteration reduces or eliminates the damping when $\theta = 0.5$. Figure 4 also shows that the damping error is directly related to the eigenvalues or more specifically $|\lambda|^n$ as indicated by Equation (62). We see that the envelope of the solution follows the curve given by $h^n = |\lambda|^n h_0$, indicating that the model behaves as theoretically predicted regarding the decay rate and the magnitude of the eigenvalues. In general, the envelope of the numerical solution does not follow $\mathbf{U}^n = \mathbf{\Lambda}^n \mathbf{U}^0$ exactly. Instead, the envelope is given by Equation (60), which involves the eigenvectors of the stability matrix. However, for this particular system, the expression $\mathbf{\Lambda}^n$ is very close to $\mathbf{X}\mathbf{\Lambda}^n\mathbf{X}^{-1}$, which is a consequence of the form of the eigenvalues and eigenvectors. Thus, we can approximate the amplitude envelope of the solution well with $h^n = |\lambda|^n h_0$ or $U^n = |\lambda|^n U_0$.

In Section 4.1, we demonstrated the unconditional stability of the linear nonhydrostatic method with pressure projection under certain conditions. Here, we demonstrate stability of the other cases by numerically evaluating the eigenvalues of the stability matrix, $\mathbf{A}$, for both the pressure projection ($\alpha = 0$) and pressure correction ($\alpha = 1$) methods with ($\beta = 0$) and without ($\beta = 1$) iteration. Recall that the stability condition is $\max(|\lambda(\mathbf{A})|) \leqslant 1$, where $\lambda(\mathbf{A})$ are the eigenvalues of $\mathbf{A}$. Figure 5 shows the magnitude of the eigenvalues for the various pressure methods as a function of θ and γ' for a nominal value of $k'\Delta t = 1$. In this figure, we only show the magnitude of the two largest eigenvalues, $|\lambda_1|$ and $|\lambda_2|$. The smallest eigenvalue of the stability matrix given in Equation (59), λ_3, is in general very close to zero and thus omitted from this analysis. The figure shows that the magnitude of the eigenvalues is less than 1 for all values of γ' when $\theta \geqslant 0.5$. The solid line in Figure 5 is the $|\lambda| = 1$ contour, which does not cross into the region where $\theta > 0.5$ for any of the methods. Therefore, the stability of all methods is dictated by the same requirement as the hydrostatic theta-method, that is, $\theta \geq 0.5$. The stability properties of projection and correction are very similar when iteration is used ($\beta = 1$), as indicated by the similarity of rows (B) and (D) in Figure 5. In fact, the critical value (neutrally stable value) of θ for stability is very close to $\theta = 0.5$ for all values of γ' when $\beta = 1$. Without iteration ($\beta = 0$), the critical value of θ is smaller for projection (Figure 5(A)) than it is for correction (Figure 5(B)) for a given value of γ', owing to the larger damping of projection over correction and of both methods over the hydrostatic θ-method. In contrast to the behavior when $\theta < 0.5$, increasing γ' when $\theta > 0.5$ leads to larger eigenvalues and less damping for increasing values of γ' because $|\lambda| \to 1$ as $\gamma' \to 1$ for correction and both iterative methods. However, when projection is used, damping is not monotonic with γ' when $\theta > 0.5$ as seen in panel (A). Instead, there exists a value of γ' in this region that maximizes the damping for λ_1 for a fixed value of θ, whereas λ_2 exhibits the most damping only when $\gamma' = 1$. We will discuss the consequences of this behavior later in this section. Figure 5 presents strong evidence of the stability of the nonhydrostatic θ-method. In what follows, we demonstrate that the method is stable for all values of $k'\Delta t$ (because Figure 5 only shows $k'\Delta t = 1$).

Figure 6 shows the magnitude of the eigenvalues of the stability matrix, $\mathbf{A}$, compared with the damping value of the fundamental mode (longest wavelength wave) extracted from the numerical experiments. This value is determined from an exponential fit to the periodic maxima of $h(x = 0, t)$. The eigenvalues of the stability matrix and the damping values from the model agree very well. The slight differences are attributable to the skill of the exponential fit to the maxima of $h(x = 0, t)$, which results in small errors on the damping values extracted from the model. Figure 6 shows that the damping for the projection method ($\alpha = 0$) is generally larger than the damping for the correction method ($\alpha = 1$) because of the higher accuracy of the correction method. The theoretical and modeled eigenvalues also approach the theoretical limits of the maximum eigenvalue as $k'\Delta t \to \infty$, which is given in Equation (65). As shown in Figure 6, the damping of the nonhydrostatic models is largest roughly at $k'\Delta t = 4$. At present, we have no explanation for this minimum, although the behavior is consistent with the limits given in Equations (65)–(67).

The analysis presented in Figure 6 is valid for the damping of the fundamental mode; however, it is informative to analyze the numerically induced damping as a function of wavenumber. The eigenvalues of the stability matrix depend on wavenumber because γ' is a function of wavenumber. As wavenumber increases, $\gamma' \to 1$, and as mentioned earlier, this corresponds to eigenvalues that are close to unity in magnitude as shown in Figure 5. Furthermore, in this case, the eigenvalues of the stability matrix are nearly independent of θ. To illustrate the effects of the grid resolution on

DOI: 10.1002/fld

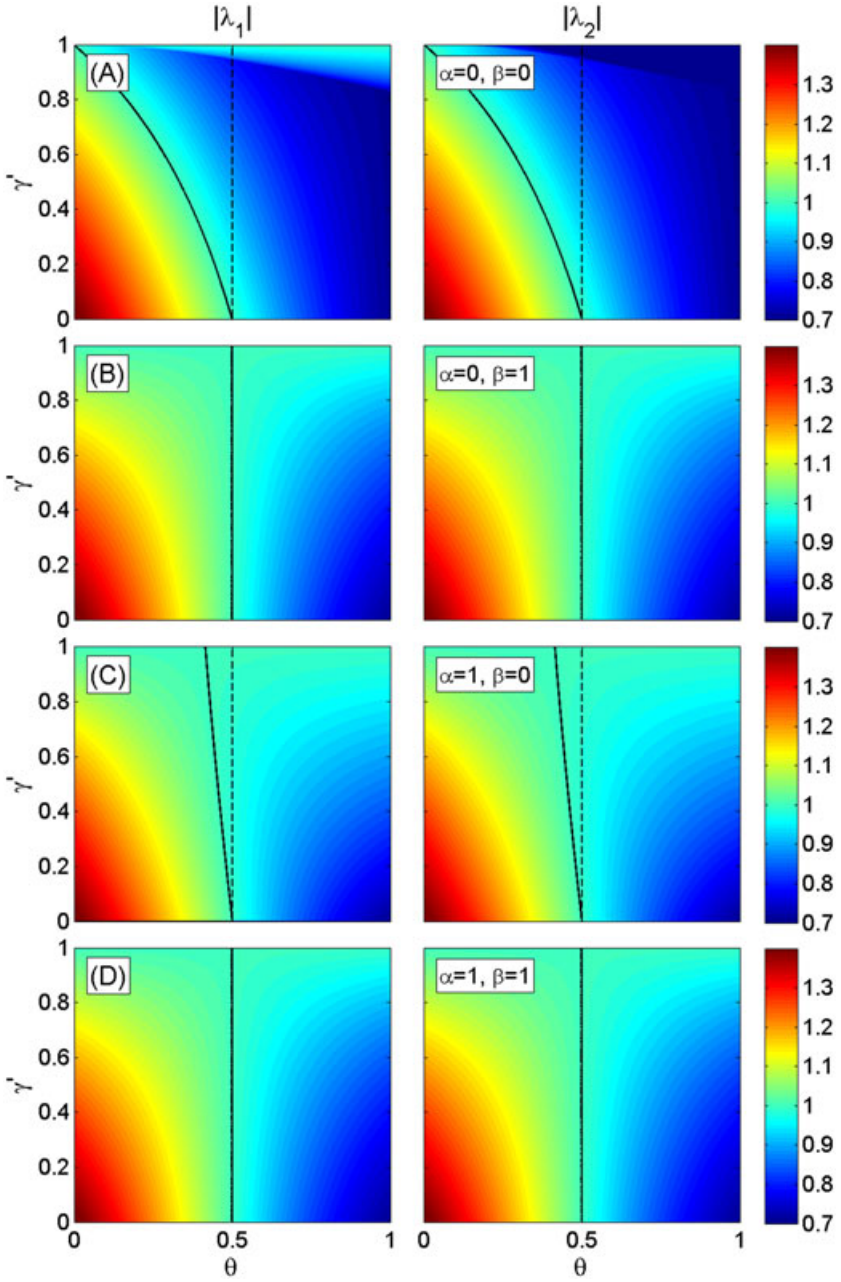

Figure 5. The eigenvalues of the pressure projection ($\alpha = 0$; panels (A) and (B)) and pressure correction ($\alpha = 1$; panels (C) and (D)) methods with ($\beta = 1$; panels (B) and (D)) and without ($\beta = 0$; panels (A) and (C)) iteration as a function of θ and γ' for $k'\Delta t = 1$. The solid line indicates $|\lambda| = 1$.

the damping, the maximum eigenvalue as a function of $k\Delta x$ is shown in Figure 7. We note that the maximum wavenumber on a discrete grid is $k_{\max} = \frac{2\pi}{2\Delta x} = \frac{\pi}{\Delta x}$, and thus, $(k\Delta x)_{\max} = \pi$. We also note that the curves shown in Figure 7 are symmetric about the y-axis, meaning this behavior holds both for positive and negative wavenumbers (i.e., right-going and left-going waves, respectively), and thus in Figure 7, we show only the positive wavenumbers. The parameters leading to the eigenvalues presented in this figure are identical to the simulations presented in Figure 6, with $k'\Delta t = 1, 10, 100$. Figure 7 shows that when $\theta = 0.5$, the nonhydrostatic methods induce more damping for low wavenumber modes than for high wavenumber modes. Furthermore, the damping

DOI: 10.1002/fld

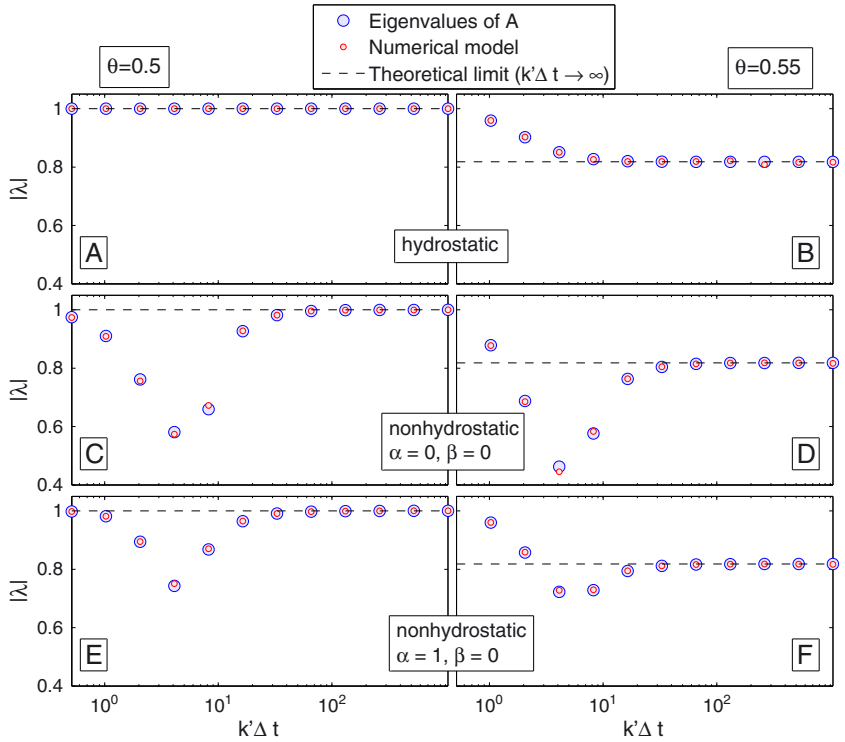

Figure 6. Damping of the fundamental mode induced by the θ-method as compared with the theoretical limit as $k'\Delta t \to \infty$. The left panels, (A), (C), and (E), illustrate the numerical damping for models with implicitness parameter $\theta = 0.5$, whereas the right panels, (B), (D), and (F), illustrate the numerical damping for models with implicitness parameter $\theta = 0.55$. Panels (A) and (B) illustrate the results of the hydrostatic model. Panels (C) and (D) illustrate the results of the nonhydrostatic model for the pressure projection method without iteration ($\alpha = 0$, $\beta = 0$). Panels (E) and (F) illustrate the results of the nonhydrostatic model for the pressure correction method without iteration ($\alpha = 1$, $\beta = 0$). The damping in all models approaches the limits for large $k'\Delta t$ given by Equation (65).

for the pressure projection method is generally larger than the correction method. In contrast to the nonhydrostatic methods, the hydrostatic method is undamped for all modes when $\theta = 0.5$. However, when $\theta = 0.55$, the hydrostatic method induces approximately constant damping value for all modes. Comparatively, the damping induced by the nonhydrostatic methods, although similar to the hydrostatic method at low wavenumbers, is significantly reduced for high wavenumbers. In fact, the damping associated with high wavenumbers is quite minimal for any value of θ or $k'\Delta t$. This is quite a significant difference between the nonhydrostatic and hydrostatic behavior of the θ-method. We interpret the physical reason for the differences in damping behavior to be the treatment of the wave speed of each mode. In the nonhydrostatic models, the dispersion or variation in wave speed with wavenumber is directly computed; thus, waves with shorter wavelength travel more slowly as they should. These slower waves are thereby better resolved by the fixed timestep, and thus, the damping is reduced. The speed of the hydrostatic waves, on the other hand, is independent of wavenumber, and thus, all wavelength waves are resolved in time in a roughly similar manner. This results in a consistent damping value for each mode. We present an example of mode-specific damping in Appendix A.

To demonstrate the possible effects of momentum advection, Figure 8 shows the two largest eigenvalues of the stability matrix when $k'\Delta t = 1$ and $\tilde{F} = 1.0 - 0.2i$, where the added imaginary component ($-ik'\Delta t F u_0 = -iFu_0 = -0.2i$) is due to the linearized scheme for advection of momentum in Equation (31) and we ignore the contribution of the vertical advection of momentum term. The added term will be purely imaginary (as earlier) when a central differencing scheme for advection of momentum is used. The magnitude of this additional term ($Fu_0 = 0.2$) is chosen to

DOI: 10.1002/fld

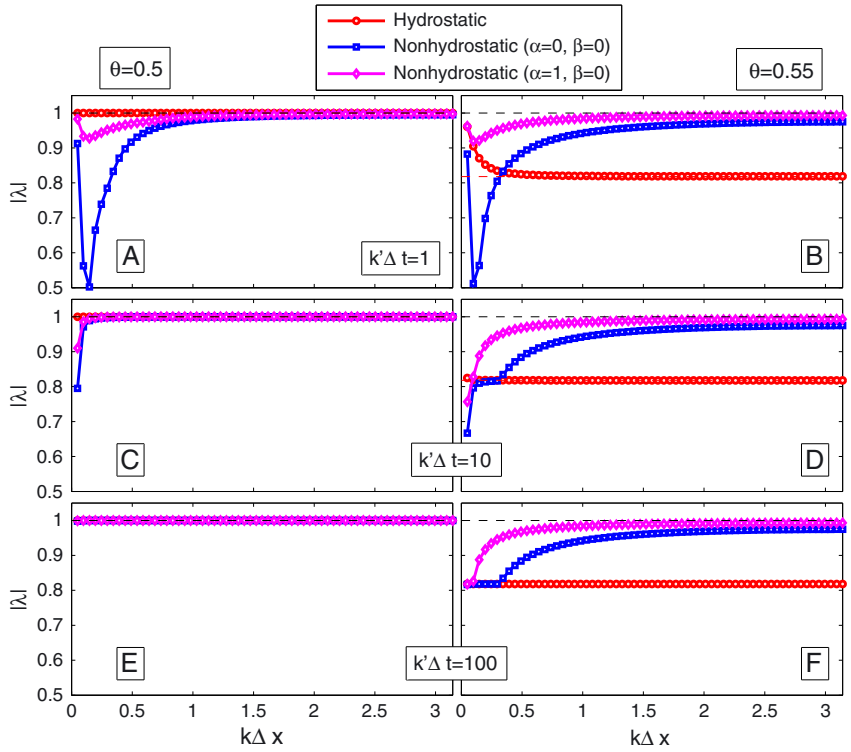

Figure 7. Damping induced by the θ-method as a function of $k\Delta x$. The left panels, (A), (C), and (E), illustrate the numerical damping of each mode for models with implicitness parameter $\theta = 0.5$, whereas the right panels, (B), (D), and (F), illustrate the numerical damping for models with implicitness parameter $\theta = 0.55$. Panels (A) and (B) illustrate the results of the models when $k'\Delta t = 1$. Panels (C) and (D) illustrate the results of the models when $k'\Delta t = 10$. Panels (E) and (F) illustrate the results of the models when $k'\Delta t = 100$.

represent the nominal case where the magnitude of the nonlinear term is approximately 20% of the linear term. As shown in Figure 8, the eigenvalues of the stability matrix $\mathbf{A}$ can be greater than unity for both the projection and correction methods, although the method is more unstable for the correction method. As mentioned earlier, the damping induced by the nonhydrostatic θ-method is minimal for high wavenumbers (with $\gamma' \approx 1$). Thus, any additional destabilizing term (such as momentum advection) may lead to high wavenumber instability because these wavenumbers are already close to the neutrally stable point where $|\lambda| = 1$. This case is shown in Figure 8 where the high wavenumber modes ($\gamma' \approx 1$) are unstable for any value of θ.

The analysis in Figure 8 informs the practice of discretizing momentum advection with a method that is unstable in the inviscid limit. Examples of this are the use of central differencing or QUICK scheme [42] in space and second-order Adams–Bashforth in time (used in [19, 43, 44], among others). In this case, the nonlinear, nonhydrostatic problem will generally experience high wavenumber instability in the inviscid limit regardless of the value of θ. These methods become stable when viscosity or some form of damping is added; however, the amount of viscosity or damping required to obtain stability is usually unknown a priori and is often tuned until the model is stable, which can possibly lead to an overly diffusive solution. This suggests the use of a time advancement scheme that is stable in the inviscid limit such as AB3 or Runge–Kutta methods (third order and higher). When these schemes are used, the stability requirements will be governed only by the advective Courant numbers.

The more common approach to discretizing advection of momentum is using an upwind, Eularian–Lagrangian method (ELM) or TVD scheme. These methods inherently induce some numerical viscosity/damping, and thus, they are stable when discretized with forward Euler time stepping. The classical method for advection of momentum used in combination with the θ-method

DOI: 10.1002/fld

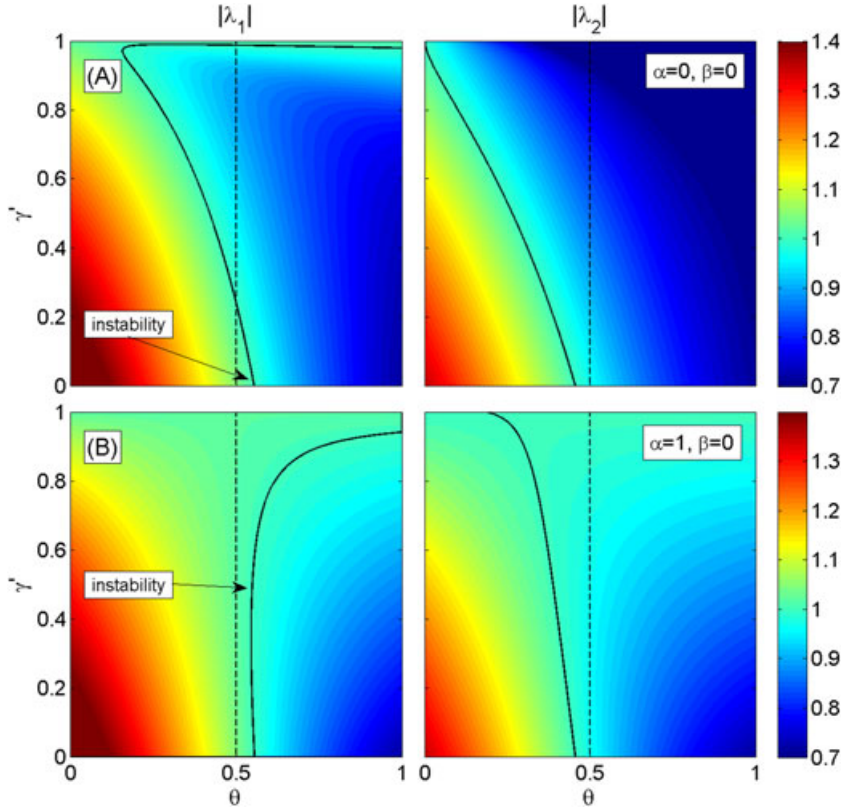

Figure 8. The eigenvalues of the pressure projection ($\alpha = 0$; top row (A)) and correction ($\alpha = 1$; bottom row (B)) methods without iteration ($\beta = 0$) as a function of θ and γ' when $\tilde{F} = 1.0 - 0.2i$ and $k'\Delta t = 1$, which represents using central differencing for advection of momentum. The solid line indicates $|\lambda| = 1$.

is ELM [1] because of its unconditional stability. In one-dimensional, when the Courant number $C \leqslant 1$, then the ELM method is identical to the upwind method as is given numerically as

$$u_{j+1/2}^{n+1} = (1 - C)u_{j+1/2}^{n} + C u_{j-1/2}^{n} , \tag{95}$$

when $u_{j+1/2}^{n} > 0$. This method is simply a linear interpolation of the velocity between the grid points $u_{j+1/2}^{n}$ and $u_{j-1/2}^{n}$ at the traceback location of the advective velocity characteristic. By using modified wavenumber analysis, the form of the operator $\tilde{F}$ based on this method is given as

$$\tilde{F} = 1 - C(1 - \cos(k\Delta x) + i \sin(k\Delta x)) . \tag{96}$$

To study the numerical damping associated with the upwind/ELM method, we perform the same eigenvalue analysis as in Figure 8 but with $\tilde{F} = 0.8 - 0.2i$. This $\tilde{F}$ parameter is determined from using a $L = 4\Delta x$ wavelength wave ($(k\Delta x) = \pi/2$) and a Courant number of $C = 0.2$ in Equation (96). This value $\tilde{F} = 0.8 - 0.2i$ is comparable with the case shown in Figure 8 but with $\mathrm{Re}\left(\tilde{F}\right) = 0.8$ instead of $\mathrm{Re}\left(\tilde{F}\right) = 1.0$. This subtle difference between the upwind/ELM method and the central differencing method is responsible for stability of the upwind/ELM method and the cost of additional damping. As shown in Figure 9, the $|\lambda| = 1$ contour is entirely in the left half-plane where $\theta < 0.5$. Thus even when $\theta = 0.5$, $|\lambda| < 1$, and there is damping associated with the method.

We conclude this section with a brief discussion on the implications of wavenumber specific damping in realistic simulations. For most tidal modeling applications, damping of high wavenumber waves will not present a serious detriment to achieving realistic simulations. Instead, proper treatment of long, low wavenumber waves is vital. However, for applications in modeling bores, fronts, or internal waves, proper representation of steep gradients and thus representation of

DOI: 10.1002/fld

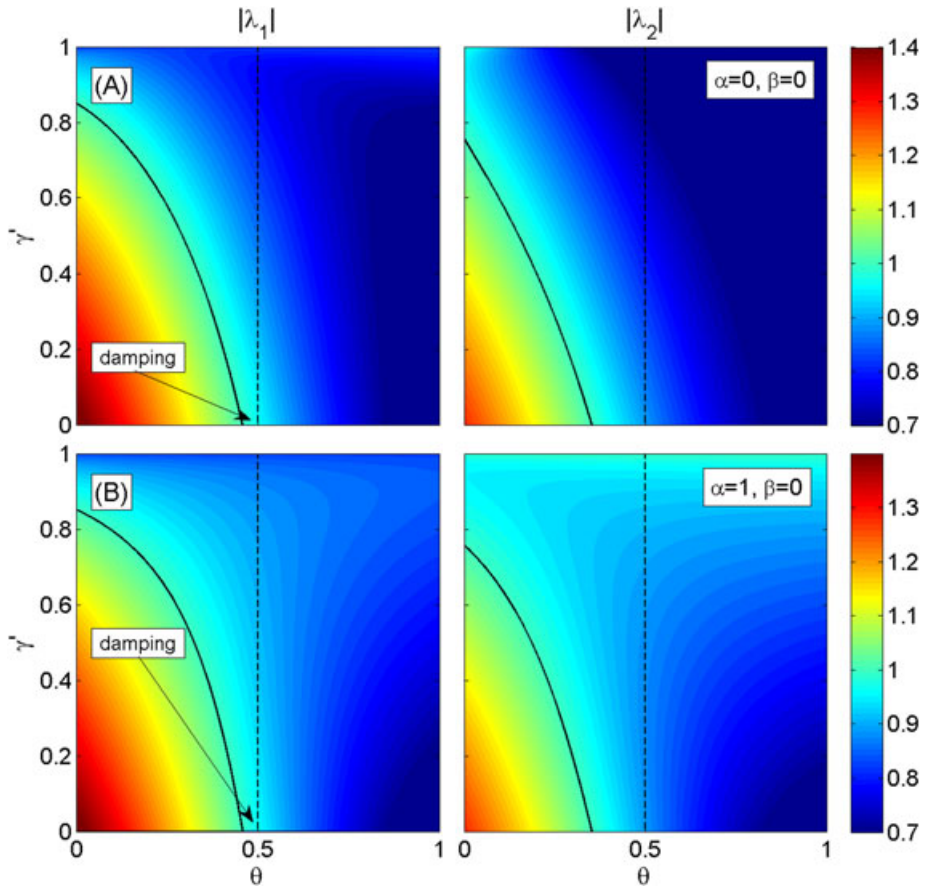

Figure 9. The eigenvalues of the pressure projection ($\alpha = 0$; top row (A)) and correction ($\alpha = 1$; bottom row (B)) methods without iteration ($\beta = 0$) as a function of θ and γ' when $\tilde{F} = 0.8 - 0.2i$ and $k'\Delta t = 1$, which represents using upwind differencing or EulerianŰLagrangian method for advection of momentum. The solid line indicates $|\lambda| = 1$.

high wavenumbers become important. To summarize the results presented in this section, modelers seeking to minimize damping of high wavenumbers should:

1. Use high-resolution or centered advection schemes with appropriate time stepping for stability.
2. Use $\theta = 0.5$ because it induces no damping at any wavenumber for the hydrostatic method.
3. When nonhydrostatic simulations are necessary, use the second-order accurate pressure correction method instead of the first-order accurate pressure projection method because the former induces significantly less damping.
4. When affordable, use iterative nonhydrostatic pressure solution methods, $\beta = 1$, because they induce no damping for all wavenumbers for the linear, inviscid equations.
5. Be mindful of how the timestep may influence damping. As shown in Figure 6, the maximum damping rate is found at approximately $k'\Delta t = 4$. However, generally speaking, decreasing the timestep should reduce the damping.

6. CONCLUSIONS

We have shown that linear, inviscid, nonhydrostatic free-surface models using the semi-implicit θ-method are unconditionally stable for surface gravity waves when $\theta \geqslant 1/2$. This implies that the overall stability requirements of a nonlinear, nonhydrostatic model reduce to the stability requirements of advection of momentum or explicit treatment of viscous terms and not the discretization of

DOI: 10.1002/fld

the nonhydrostatic pressure. Therefore, there is no timestep restriction associated with computing the nonhydrostatic pressure. However, the nonhydrostatic methods can give rise to artificial damping of the free surface. For nonhydrostatic models using the first-order accurate pressure projection method, the low wavenumber modes of the free surface are damped even when $\theta = 0.5$. Alternatively, using the second-order accurate pressure correction method induces much less damping. The hydrostatic θ-method damps all wavenumber waves at roughly the same rate when $\theta > 0.5$. However, damping of high wavenumber modes of the nonhydrostatic θ-method is significantly reduced compared with the damping induced by the hydrostatic model.

APPENDIX A: WAVENUMBER DEPENDENT DAMPING

In this analysis, we verify that the theoretical behavior for wavenumber dependent damping shown in Figure 7 holds in numerical experiments. Figure A.1 demonstrates wavenumber dependent damping of a nonhydrostatic simulation with a stable $\theta = 0.5$ and with $C = 20$ and $k'\Delta t = 1$. In this case, all of the modes are stable (amplification factor: $\sigma < 1$) and hence are damped in time, albeit at different rates. The initial condition for this numerical experiment is $h_0 = 0.25\cos(k_1 x) + 1\cos(k_2 x) + 0.5\cos(k_3 x) + 0.75\cos(k_4 x)$. These wavenumbers (k_1, k_2, k_3, k_4) are

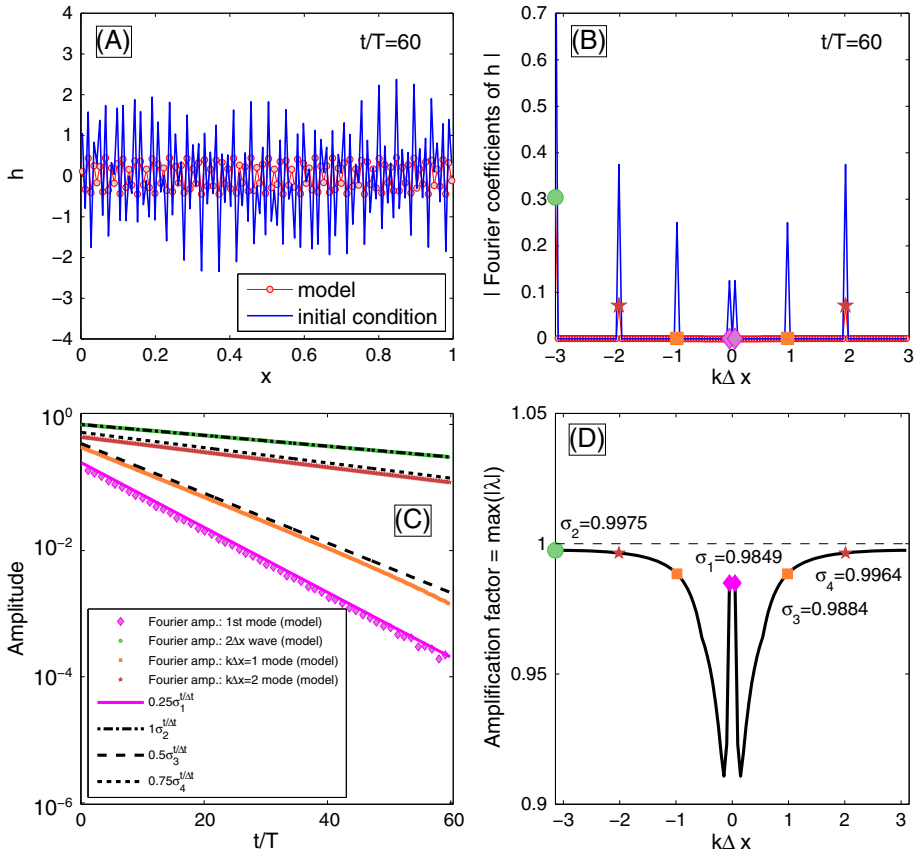

Figure A.1. The numerical damping of the various wave modes over the course of a stable nonhydrostatic ($\alpha = 1, \beta = 0$) simulation with $\theta = 0.5$. Panel (A) shows the initial condition compared with the numerical solution at $t/T = 60$. Panel (B) shows the magnitude of the Fourier coefficients of the initial condition and final numerical solution at time $t/T = 60$ in panel (A) as a function of $k\Delta x$. Panel (D) shows the amplification factor (the maximum eigenvalue) of the stability matrix for this system as a function of $k\Delta x$. Panel (C) shows the comparison of the Fourier amplitudes of the fundamental, $2\Delta x$ (wavelength), $k\Delta x = 1$, and $k\Delta x = 2$ waves as compared with the expressions $0.25(\sigma_1)^{t/\Delta t}$, $1 \times 10^{-17}(\sigma_2)^{t/\Delta t}$, $0.5(\sigma_3)^{t/\Delta t}$, and $0.75 \times 10^{-10}(\sigma_4)^{t/\Delta t}$, respectively, which are derived from the amplification factors in panel (D).

DOI: 10.1002/fld

chosen so that the smallest and the largest $k\Delta x$ waves ($k_1 = \pi/L$ and $k_2 = \pi/\Delta x$, respectively) are investigated as well as waves with $k_3\Delta x = 1$ and $k_4\Delta x = 2$. The amplitudes are chosen for plotting purposes. In Figure A.1(B), the Fourier coefficients of the initial condition and modeled solution at time $t/T = 60$ are plotted against $k\Delta x$. We extract the Fourier coefficients corresponding to wavenumbers k_1, k_2, k_3, and k_4, respectively, at each timestep of the model to determine their damping rate throughout the simulation.[‡] We also determine their approximate amplification/damping factor analytically (i.e., σ_1, σ_2, σ_3, and σ_4) from the maximum (in absolute value) of the eigenvalues of the stability matrix. Figure A.1(D) shows the amplification/damping factor as a function of wavenumber derived from the eigenvalue analysis. Thus, we can compare the damping predicted by the theoretically derived amplification factor to that of the local maxima of the extracted Fourier amplitudes over the course of this simulation. This comparison is shown in Figure A.1(C), which demonstrates that the damping of the waves in the model can be reproduced using the simple expressions $1(\sigma_1)^{t/\Delta t}$, $1\times10^{-17}(\sigma_2)^{t/\Delta t}$, $1(\sigma_3)^{t/\Delta t}$, and $1\times10^{-10}(\sigma_4)^{t/\Delta t}$.

APPENDIX B: STABILITY OF THE VELOCITY PERTURBATION

In the preceding sections, the depth-averaged velocity, U, and the free-surface height, h, are demonstrated to be unconditionally stable when discretized using the θ-method. In this appendix, we show that the velocity perturbation, the deviation from the depth-averaged velocity, $u' = u - U$, cannot increase without bound and is thus also unconditionally stable.

The depth-averaged velocity following Equation (43) is given as

$$U^{n+1} = U^n - i\theta k'\Delta t h^{n+1} - i\,(1-\theta)\,k'\Delta t h^n - ik'\Delta t\Delta z\mathbf{e}^T\mathbf{q}^{n+1/2}\,, \tag{B.1}$$

where we assume that the problem is linear, $\tilde{F} = 1$. Likewise, the full (nondepth-averaged velocity) is given as

$$\mathbf{u}^{n+1} = \mathbf{u}^n - i\theta k'\Delta t h^{n+1}\mathbf{e} - i\,(1-\theta)\,k'\Delta t h^n\mathbf{e} - ik'\Delta t\mathbf{q}^{n+1/2}\,. \tag{B.2}$$

Subtracting $\mathbf{e}$ times Equation (B.1) from Equation (B.2), we obtain an expression for the velocity perturbation, which is given as

$$(\mathbf{u}')^{n+1} = (\mathbf{u}')^n - ik'\Delta t\left(\Delta z\mathbf{e}\mathbf{e}^T - \mathbf{I}\right)\mathbf{q}^{n+1/2}\,, \tag{B.3}$$

where $\mathbf{u}' = \mathbf{u} - U\mathbf{e}$. Substituting Equation (47) for the nonhydrostatic pressure, $\mathbf{q}^{n+1/2}$, into Equation (B.3) , the velocity perturbation can be written as

$$(\mathbf{u}')^{n+1} = (\mathbf{u}')^n - ik'\Delta t\left(\theta h^{n+1} + (1-\theta)h^n\right)\mathbf{B}\mathbf{e}\,, \tag{B.4}$$

where

$$\mathbf{B} = \left(\Delta z\mathbf{e}\mathbf{e}^T - \mathbf{I}\right)\left(\mathbf{I} + \left(k'\epsilon\right)^{-2}\mathbf{M}\right)^{-1} = \left(\Delta z\mathbf{e}\mathbf{e}^T - \mathbf{I}\right)\mathbf{C}\,, \tag{B.5}$$

and thus,

$$\begin{aligned}\mathbf{B}\mathbf{e} &= \Delta z\mathbf{e}\mathbf{e}^T C\mathbf{e} - \mathbf{C}\mathbf{e}\\ &= \mathbf{e}(\Delta z\mathbf{e}^T C\mathbf{e}) - \mathbf{C}\mathbf{e}\\ &= \gamma'\mathbf{e} - \mathbf{C}\mathbf{e}\\ &= \gamma'\mathbf{e} + \boldsymbol{\phi}'\,,\end{aligned}$$

where $\boldsymbol{\phi}' = -\mathbf{C}\mathbf{e}$ is the discrete structure function given in Equation (49).

[‡]We note that because the solution is a standing wave, the amplitude of the Fourier coefficients will oscillate throughout the course of the simulation; thus, it is necessary to analyze only the local maxima of the Fourier amplitudes in time.

DOI: 10.1002/fld

The norm of Equation (B.4) is given as

$$\begin{aligned}||(\mathbf{u}')^{n+1}|| &= ||(\mathbf{u}')^{n} - ik'\Delta t(\theta h^{n+1} + (1-\theta)h^{n})\mathbf{Be}|| \\ &\leqslant ||(\mathbf{u}')^{n}|| + ||-ik'\Delta t(\theta h^{n+1} + (1-\theta)h^{n})\mathbf{Be}|| \\ &\leqslant ||(\mathbf{u}')^{n}|| + |ik'\Delta t(\theta h^{n+1} + (1-\theta)h^{n})|\,||\mathbf{Be}|| \\ &\leqslant ||(\mathbf{u}')^{n}|| + k_n||\mathbf{Be}||\,, \end{aligned} \tag{B.6}$$

where $k_n = |ik'\Delta t(\theta h^{n+1} + (1-\theta)h^{n})|$. The recurrence relation, Equation (B.6), can be written in terms of the initial velocity perturbation, $(\mathbf{u}')^0$, and the initial free-surface height, h^0 , as

$$||(\mathbf{u}')^{n}|| \leqslant ||(\mathbf{u}')^{0}|| - ||\mathbf{Be}|| \sum_{p=0}^{n} k_p\,. \tag{B.7}$$

In the previous sections, we showed that the evolution of the free-surface height can be expressed as $h^p = \sigma^p h^0$, where σ is the amplification factor and $|\sigma| < 1$. Substituting this expression for h^p into the expression for k_p gives

$$\begin{aligned} k_p &= |i(k'\Delta t)\left(\theta\sigma^{p+1}h^0 + (1-\theta)\sigma^p h^0\right)| \\ &= |i(k'\Delta t)\left(\theta\sigma\sigma^p h^0 + (1-\theta)\sigma^p h^0\right)| \\ &= |i(k'\Delta t)(1+\theta\sigma-\theta)h^0|\,|\sigma^p| \\ &= c_1|\sigma^p|\,, \end{aligned} \tag{B.8}$$

where $c_1 = |i(k'\Delta t)(1+\theta\sigma-\theta)h^0|$. Thus, Equation (B.7) can be written as

$$||(\mathbf{u}')^{n}|| \leqslant ||(\mathbf{u}')^{0}|| + c_1||\mathbf{Be}|| \sum_{p=0}^{n} |\sigma^p|\,. \tag{B.9}$$

The summation $\sum_{p=0}^{n} |\sigma^p|$ in Equation (B.9) converges because $|\sigma| < 1$. Thus, we can write the perturbation velocity at time ∞ as

$$||(\mathbf{u}')^{\infty}|| \leqslant ||(\mathbf{u}')^{0}|| + c_2||\mathbf{Be}||, \tag{B.10}$$

where $c_2 = c_1 \sum_{p=0}^{\infty} |\sigma^p|$. Because the summation in the expression for c_2, the initial velocity perturbation $||(\mathbf{u}')^0||$, and $||\mathbf{Be}||$ are finite, then the norm of the perturbation velocity at any time step is bounded and thus the full velocity ($u = u' + U$) is unconditionally stable when discretized with the θ-method when $\theta \geqslant 0.5$.

APPENDIX C: ORDER OF ACCURACY ESTIMATES

In this appendix, we follow the order of accuracy analysis presented in [38], which is extended to include an examination of the convergence behavior of the iterative method ($\beta = 1$). We determine the order of accuracy of the discrete form of governing Equations (27) and (29), which are given by

$$\frac{\mathbf{u}^{n+1} - \mathbf{u}^{n}}{\Delta t} = -\theta\mathbf{e}G_x h^{n+1} - (1-\theta)\,\mathbf{e}G_x h^{n} - G_x\mathbf{q}_c^{n+1/2} - \alpha G_x\mathbf{q}^{n-1/2}\,, \tag{C.1}$$

$$\frac{h^{n+1} - h^{n}}{\Delta t} = -\theta\Delta z D_x\mathbf{e}^T\mathbf{u}^{n+1} - (1-\theta)\Delta z D_x\mathbf{e}^T\mathbf{u}^{n}. \tag{C.2}$$

Here, we only consider error of the nonhydrostatic free-surface method (i.e., we ignore the effects of advection, diffusion, or other terms). Following the solution procedure given in Section 3, Equations (C.1) and (C.2) can be split into the hydrostatic predictor and nonhydrostatic corrector parts as

$$\frac{\mathbf{u}^{*} - \mathbf{u}^{n}}{\Delta t} = -\theta\mathbf{e}G_x h^{*} - (1-\theta)\,\mathbf{e}G_x h^{n} - \alpha G_x\mathbf{q}^{n-1/2}\,, \tag{C.3}$$

DOI: 10.1002/fld

$$\frac{h^* - h^n}{\Delta t} = -\theta \Delta z D_x \mathbf{e}^T \mathbf{u}^* - (1-\theta)\Delta z D_x \mathbf{e}^T \mathbf{u}^n, \tag{C.4}$$

and

$$\frac{\mathbf{u}^{n+1} - \mathbf{u}^*}{\Delta t} = -G_x \mathbf{q}_c^{n+1/2}\,, \tag{C.5}$$

$$\frac{h^{n+1} - h^*}{\Delta t} = \beta\theta \Delta t \Delta z L_{xx} \mathbf{e}^T \mathbf{q}_c^{n+1/2}, \tag{C.6}$$

respectively. Equations (C.5) and (C.6) can be rearranged as

$$\mathbf{u}^* = \mathbf{u}^{n+1} + \Delta t G_x \mathbf{q}_c^{n+1/2}\,, \tag{C.7}$$

$$h^* = h^{n+1} - \beta\theta \Delta t^2 \Delta z L_{xx} \mathbf{e}^T \mathbf{q}_c^{n+1/2}. \tag{C.8}$$

Substituting Equations (C.7) and (C.8) into Equations (C.3) and (C.4), we obtain

$$\frac{\mathbf{u}^{n+1} - \mathbf{u}^n}{\Delta t} = -\theta \mathbf{e} G_x h^{n+1} - (1-\theta)\,\mathbf{e} G_x h^n - G_x \mathbf{q}^{n+1/2} + \beta\theta^2 \Delta t^2 \Delta z \mathbf{e} G_x L_{xx} \mathbf{e}^T \mathbf{q}_c^{n+1/2}\,, \tag{C.9}$$

$$\frac{h^{n+1} - h^n}{\Delta t} = -\theta \Delta z D_x \mathbf{e}^T \mathbf{u}^{n+1} - (1-\theta)\Delta z D_x \mathbf{e}^T \mathbf{u}^n - (1-\beta)\theta \Delta t \Delta z L_{xx} \mathbf{e}^T \mathbf{q}_c^{n+1/2}. \tag{C.10}$$

Substituting

$$\begin{aligned} \mathbf{q}_c^{n+1/2} = \mathbf{q}^{n+1/2} - \alpha \mathbf{q}^{n-1/2} &= \begin{cases} \mathbf{q}^{n+1/2} - \mathbf{q}^{n-1/2} = \Delta t \frac{\partial \mathbf{q}}{\partial t} + \mathcal{O}(\Delta t^2), & \text{if } \alpha = 1 \\ \mathbf{q}^{n+1/2}, & \text{if } \alpha = 0 \end{cases} \\ &= \alpha \left(\Delta t \frac{\partial \mathbf{q}}{\partial t} + \mathcal{O}(\Delta t^2) \right) + (1-\alpha)\mathbf{q}^{n+1/2} \end{aligned} \tag{C.11}$$

into Equations (C.9) and (C.10) gives

$$\begin{aligned} \frac{\mathbf{u}^{n+1} - \mathbf{u}^n}{\Delta t} &= -\theta \mathbf{e} G_x h^{n+1} - (1-\theta)\,\mathbf{e} G_x h^n - G_x \mathbf{q}^{n+1/2} \\ &\quad + (1-\alpha)\beta\theta^2 \Delta t^2 \Delta z \mathbf{e} G_x L_{xx} \mathbf{e}^T \mathbf{q}^{n+1/2} + \alpha\beta\theta^2 \Delta t^3 \Delta z \mathbf{e} G_x L_{xx} \mathbf{e}^T \frac{\partial \mathbf{q}}{\partial t} + \mathcal{O}\left(\Delta t^4\right) \\ &= -\theta \mathbf{e} G_x h^{n+1} - (1-\theta)\,\mathbf{e} G_x h^n - G_x \mathbf{q}^{n+1/2} \\ &\quad + \beta\left[(1-\alpha)\mathcal{O}\left(\Delta t^2\right) + \alpha\mathcal{O}\left(\Delta t^3\right) + \mathcal{O}\left(\Delta t^4\right)\right], \end{aligned} \tag{C.12}$$

$$\begin{aligned} \frac{h^{n+1} - h^n}{\Delta t} &= -\theta \Delta z D_x \mathbf{e}^T \mathbf{u}^{n+1} - (1-\theta)\Delta z D_x \mathbf{e}^T \mathbf{u}^n \\ &\quad - (1-\alpha)(1-\beta)\theta \Delta t \Delta z L_{xx} \mathbf{e}^T \mathbf{q}^{n+1/2} - \alpha(1-\beta)\theta \Delta t^2 \Delta z L_{xx} \mathbf{e}^T \frac{\partial \mathbf{q}^{n+1/2}}{\partial t} + \mathcal{O}\left(\Delta t^3\right) \\ &= -\theta \Delta z D_x \mathbf{e}^T \mathbf{u}^{n+1} - (1-\theta)\Delta z D_x \mathbf{e}^T \mathbf{u}^n \\ &\quad - (1-\beta)\left[(1-\alpha)\mathcal{O}(\Delta t) + \alpha\mathcal{O}\left(\Delta t^2\right) + \mathcal{O}\left(\Delta t^3\right)\right]. \end{aligned} \tag{C.13}$$

Thus, we see that the nonhydrostatic projection method induces an error of $\mathcal{O}(\Delta t)$ in free-surface Equation (C.13) when $\alpha = 0$ and $\beta = 0$. When $\alpha = 1$ or $\beta = 1$, then the method becomes at least second-order accurate. We note that the aforementioned analysis only considers the error induced by the nonhydrostatic projection part of the method. As discussed in [3], the (hydrostatic portion) of the θ-method for the free surface is second-order accurate when $\theta = 0.5$ and first-order accurate otherwise. We also note that the eigenvalue analysis discussed in Section 4.2 can be used to estimate the time accuracy of the methods. In the following analysis, we verify the order of accuracy with numerical experiments.

DOI: 10.1002/fld

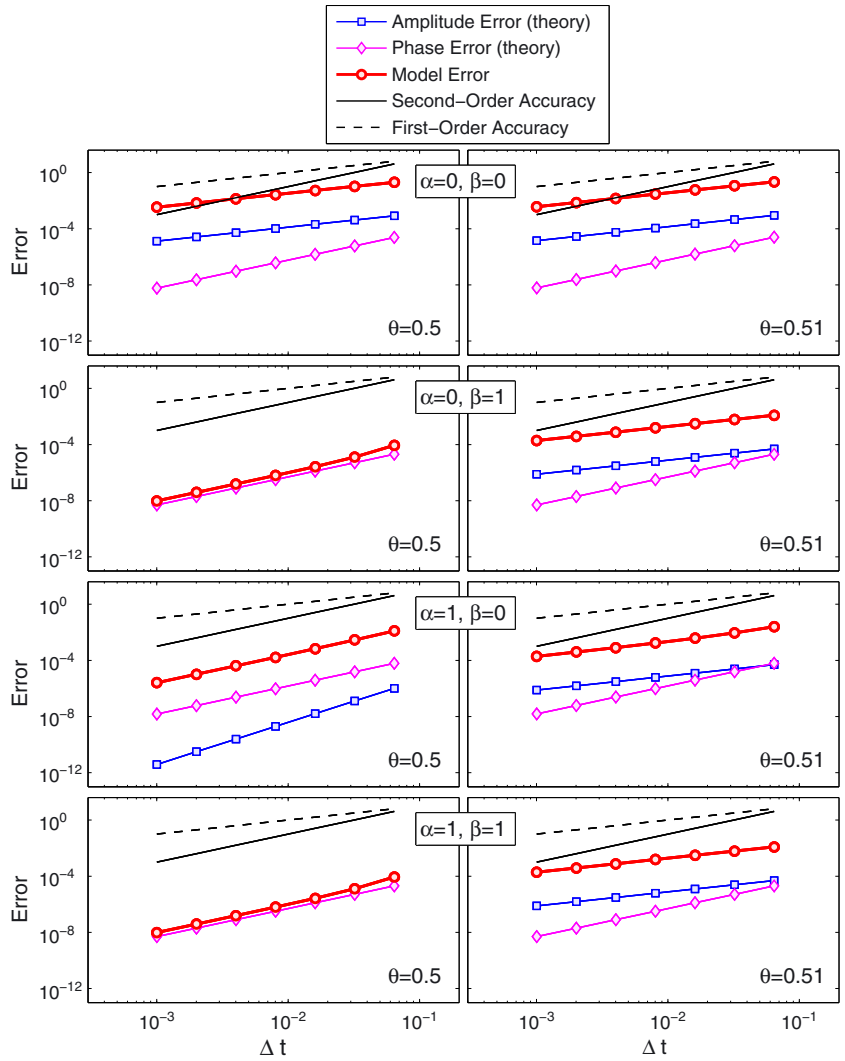

Figure C.1. The error of the nonhydrostatic θ-method as compared with the amplitude and dispersive error estimates from the eigenvalues of the stability matrix as a function of Δt. The left panels show the order of accuracy estimates for $\theta = 0.5$, whereas the right panels show the order of accuracy estimates for $\theta = 0.51$. The method is only first-order accurate when $\theta = 0.5$, $\alpha = 0$, and $\beta = 0$. The overall order of accuracy of the model corresponds to the lessor of the order of accuracy of the amplitude or dispersive error as predicted by the eigenvalue analysis.

Figure C.1 shows the model error as a function Δt. The error is computed as $||h(\Delta t) - h(\Delta t/2)||_2$, where $h(\Delta t)$ represents the numerical solution of the free surface, h, computed with a timestep of Δt after one period $t_{\max} = T$. We compare the convergence of the model error with the convergence of the theoretically estimated amplitude and phase errors given by Equations (74) and (75), respectively. The convergence experiments are run with the same numerical parameters and initial conditions as in Figure 4, for both the projection ($\alpha = 0$) and correction ($\alpha = 1$) methods with ($\beta = 1$) and without iteration ($\beta = 0$) with $\theta = 0.5, 0.51$. As shown in Figure C.1, the overall model order of accuracy behaves as the lessor of the order of accuracy of the amplitude or phase error. For all methods, the theoretical estimate for the phase error is roughly second-order accurate; however, when $\theta = 0.51$ and for the projection method without iteration ($\alpha = 0$, $\beta = 0$) with $\theta = 0.5$, the amplitude error and thus the overall modeled error are only first-order accurate at best. Even when $\theta = 0.5$, the numerical solution of the nonhydrostatic pressure for $\alpha = 0$, $\beta = 0$ is only first-order in time, and thus overall, the method is only first-order accurate in time.

DOI: 10.1002/fld

This result agrees with the analysis in [38] and Equation (C.13). Furthermore, when $\alpha = 1$ and $\theta = 0.5$, both the free-surface discretization and the nonhydrostatic pressure are second-order accurate, and thus, the model is second-order accurate.

APPENDIX D: CONVERGENCE OF THE ITERATIVE ($\beta = 1$) NONHYDROSTATIC METHOD

In this section, we investigate the convergence properties of the linear iterative ($\beta = 1$) nonhydrostatic method. We begin with the linear advancement equations of the numerical method that are closely related to Equations (43) and (44), viz.

$$\begin{aligned} U^{n+1} = U^n - i\theta k'\Delta t h^{n+1} - i\left(1-\theta-\alpha\gamma'\theta\right)k'\Delta t h^n \\ + i\alpha\gamma'(1-\theta)k'\Delta t h^{n-1} - ik'\Delta t\Delta z\mathbf{e}^T\mathbf{q}_c^{n+1/2}\,, \end{aligned} \tag{D.1}$$

$$\begin{aligned} \left(1+\theta^2(k'\Delta t)^2\right)h^{n+1} = -ik'\Delta t U^n + \left(1-\theta\,(1-\theta)\,(k'\Delta t)^2 + \alpha\gamma'\theta^2(k'\Delta t)^2\right)h^n \\ + \alpha\gamma'\theta(1-\theta)(k'\Delta t)^2 h^{n-1} - \beta\theta(k'\Delta t)^2\Delta z\mathbf{e}^T\mathbf{q}_c^{n+1/2}\,. \end{aligned} \tag{D.2}$$

Equations (D.1) and (D.2) are split into the hydrostatic predictor part

$$\begin{aligned} U^* = U^n - i\theta k'\Delta t h^{n+1} - i\left(1-\theta-\alpha\gamma'\theta\right)k'\Delta t h^n \\ + i\alpha\gamma'(1-\theta)k'\Delta t h^{n-1}\,, \end{aligned} \tag{D.3}$$

$$\begin{aligned} h^* = -i\left(1+\theta^2(k'\Delta t)^2\right)^{-1}k'\Delta t U^n \\ + \left(1+\theta^2(k'\Delta t)^2\right)^{-1}\left(1-\theta\,(1-\theta)\,(k'\Delta t)^2 + \alpha\gamma'\theta^2(k'\Delta t)^2\right)h^n \\ + \alpha\gamma'\theta(1-\theta)\left(1+\theta^2(k'\Delta t)^2\right)^{-1}(k'\Delta t)^2 h^{n-1} \end{aligned} \tag{D.4}$$

and nonhydrostatic corrector part

$$U^{n+1} = U^* - ik'\Delta t\Delta z\mathbf{e}^T\mathbf{q}_c^{n+1/2}\,, \tag{D.5}$$

$$h^{n+1} = h^* - \beta\theta\left(1+\theta^2(k'\Delta t)^2\right)^{-1}(k'\Delta t)^2\Delta z\mathbf{e}^T\mathbf{q}_c^{n+1/2}\,, \tag{D.6}$$

where U^* and h^* represent the provisional (hydrostatic) velocity and free surface, respectively. The nonhydrostatic correction is performed after the solution of Poisson Equation (47), viz.

$$\mathbf{q}_c^{n+1/2} = -\mathbf{Ce}\left(\theta h^{n+1} + (1-\theta)h^n\right)\,, \tag{D.7}$$

where $\mathbf{C} = \left[\mathbf{I} + (k'\epsilon)^2\mathbf{M}\right]^{-1}$. However, in general, the final nonhydrostatic free-surface height $\left(h^{n+1}\right)$ is not known without iteration. Instead, the Poisson equation is given as

$$\mathbf{q}_c^{(m)} = -\mathbf{Ce}\left(\theta h^{(m)} + (1-\theta)h^n\right)\,, \tag{D.8}$$

where the superscript (m) indicates the iteration number. Similarly, we write Equation (D.8) in depth-averaged from as

$$\Delta z\mathbf{e}^T\mathbf{q}_c^{(m)} = -\Delta z\mathbf{e}^T\mathbf{Ce}\left(\theta h^{(m)} + (1-\theta)h^n\right) = -\gamma'\left(\theta h^{(m)} + (1-\theta)h^n\right)\,, \tag{D.9}$$

where $\gamma' = \Delta z\mathbf{e}^T\mathbf{Ce}$ from Equation (50). The free-surface equation also requires an iterative solution

$$h^{(m+1)} = h^* - \beta\theta\left(1+\theta^2(k'\Delta t)^2\right)^{-1}(k'\Delta t)^2\Delta z\mathbf{e}^T\mathbf{q}_c^{(m)}\,. \tag{D.10}$$

DOI: 10.1002/fld

Note that if $\beta = 0$, then there is no iteration, and $h^{n+1} = h^*$ according to Equation (D.6). Substituting nonhydrostatic correction iterate (D.9) into free-surface iterate (D.10), we obtain a recurrence relation for the free surface given by

$$h^{(m+1)} = h^{**} + \mu h^{(m)} , \tag{D.11}$$

where $\mu \equiv \beta\gamma' \frac{\theta^2(k'\Delta t)^2}{1+\theta^2(k'\Delta t)^2}$ and $h^{**} = h^* + \beta\gamma' \frac{\theta(1-\theta)(k'\Delta t)^2}{1+\theta^2(k'\Delta t)^2} h^n$. With this recurrence relation, we derive a formula for the mth iteration step as a function of the starting value $h^{(0)} = h^*$, which is given by

$$h^{(m)} = \mu^m h^{(0)} + h^{**} \sum_{i=0}^{m-1} \mu^i . \tag{D.12}$$

Using Equation (D.12), we obtain the convergence rate by subtracting $h^{(m)}$ from $h^{(m+1)}$, which gives

$$h^{(m+1)} - h^{(m)} = \mu^m h^{***} , \tag{D.13}$$

where $h^{***} = \beta\gamma' \frac{\theta(k'\Delta t)^2}{1+\theta^2(k'\Delta t)^2} (\theta h^* + (1-\theta)h^n)$. Thus, Equation (D.13) shows that the iteration converges with powers of $\mu \equiv \beta\gamma' \frac{\theta^2(k'\Delta t)^2}{1+\theta^2(k'\Delta t)^2}$. This parameter is always less than unity, and thus, the iteration is guaranteed to converge. Also of note is that the iteration converges rapidly for small values of $k'\Delta t$ and for flows that are nearly hydrostatic ($\gamma' \ll 1$).

We estimate error reduction associated with the iteration by subtracting Equation (D.10) from (D.6) to give

$$h^{n+1} - h^{(m+1)} = \mu \left(h^{n+1} - h^{(m)} \right) . \tag{D.14}$$

This result generalizes to

$$h^{n+1} - h^{(m)} = \mu^m \left(h^{n+1} - h^{(0)} \right) = \mu^m \left(h^{n+1} - h^* \right) , \tag{D.15}$$

where $h^{n+1} - h^*$ (given by Equation (C.6)) is the error committed from using the noniterative method for the free surface. This result shows that the error is systematically reduced by a factor μ each iteration.

We can also determine the approximate number of iterations until convergence is reached by setting tolerance $= h^{(m+1)} - h^{(m)}$ and using Equation (D.13) to solve for m, which gives

$$m = \frac{\log(\text{tolerance}) - \log(h^{***})}{\log(\mu)} . \tag{D.16}$$

If we assume that $\log(h^{***}) = \mathcal{O}(1)$ and consequently $|\log(\text{tolerance})| \gg |\log(h^{***})|$, then we can simplify this formula to

$$m \approx \frac{\log(\text{tolerance})}{\log(\mu)} . \tag{D.17}$$

Equation (D.17) does not depend on the magnitude of the initial condition (as Equation (D.16) does) and will still provide a good indication of the number of iterations required for convergence. Generally speaking, a simulation with $k'\Delta t = 1$ and $\theta = 0.5$ requires about 14 iterations to converge to a tolerance of 1×10^{-10} for even the slowest converging case where $\gamma' \approx 1$. Finally, we note that the overall order of accuracy does not change with ($\beta = 1$) or without ($\beta = 0$) the use of iteration when the pressure correction method is used ($\alpha = 1$) as shown in Appendix C. Using iteration with the first-order accurate pressure projection method ($\alpha = 0$) will provide the overall second-order accuracy at the cost of increased computational effort. The choice of the maximum iteration number or convergence tolerance will only influence the order of accuracy if the first-order

DOI: 10.1002/fld

accurate projection method ($\alpha = 0$) is used. Using either pressure method, the choice of maximum iteration number or convergence tolerance when using the iterative method should not influence the stability of the method because the error in Equation (D.15) is systematically reduced to zero by a constant factor μ each successive iteration and the method is stable with or without the presence of this error.

ACKNOWLEDGEMENTS

SV gratefully acknowledges his support as a Department of Energy Computational Science Graduate Fellow, which is provided under grant number DE-FG02-97ER25308. SV and OBF gratefully acknowledge the support of ONR as part of the YIP and PECASE awards under grants N00014-10-1-0521 and N00014-08-1-0904 (scientific officers Dr. C. Linwood Vincent, Dr. Terri Paluszkiewicz, and Dr. Scott Harper). We also thank two anonymous reviewers for their comments and suggestions that led to a significant improvement of the manuscript.

REFERENCES

1. Casulli V, Cheng RT. Semi-implicit finite difference methods for three-dimensional shallow water flow. *International Journal for Numerical Methods in Fluids* 1992; **15**(6):629–648.
2. Crank J, Nicolson P. A practical method for numerical evaluation of solutions of partial differential equations of the heat-conduction type. *Mathematical Proceedings of the Cambridge Philosophical Society* 1947; **43**(01):50–67.
3. Casulli V, Cattani E. Stability, accuracy and efficiency of a semi-implicit method for three-dimensional shallow water flow. *Computers and Mathematics with Applications* 1994; **27**(4):99–112.
4. Dahlquist GG. A special stability problem for linear multistep methods. *BIT Numerical Mathematics* 1963; **3**:27–43. 10.1007/BF01963532.
5. Moin P. *Fundamentals of Engineering Numerical Analysis*. Cambridge University Press: Cambridge, 2001.
6. Casulli V. A semi-implicit finite difference method for non-hydrostatic, free-surface flows. *International Journal for Numerical Methods in Fluids* 1999a; **30**:425–440.
7. Dukowicz JK, Smith RD. Implicit free-surface method for the Bryan-Cox-Semtner ocean model. *Journal of Geophysical Research* 1994; **99**:7991–8014.
8. Mahadevan A, Oliger J, Street R, A nonhydrostatic mesoscale ocean model. Part II: numerical implementation. *Journal of Physical Oceanography* 1996b; **26**:1880–1900.
9. Marshall J, Adcroft A, Hill C, Perelman L, Heisey C. A finite-volume, incompressible navier stokes model for studies of the ocean on parallel computers. *Journal of Geophysical Research* 1997; **102**:5753–5766.
10. Hodges BR. Numerical techniques in CWR-ELCOM. *Technical Report no. WP 1422-BH*, Centre for Water Research, University of Western Australia, 2000.
11. Stelling GS, Busnelli MM. Numerical simulation of the vertical structure of discontinuous flows. *International Journal for Numerical Methods in Fluids* 2001; **37**(1):23–43.
12. Namin MM, Lin B, Falconer RA. An implicit numerical algorithm for solving non-hydrostatic free-surface flow problems. *International Journal for Numerical Methods in Fluids* 2001; **35**(3):341–356.
13. Casulli V, Walters R. An unstructured grid, three-dimensional model based on the shallow water equations. *International Journal for Numerical Methods in Fluids* 2000; **32**:331–348.
14. Casulli V, Zanolli P. Semi-implicit numerical modeling of nonhydrostatic free-surface flows for environmental problems. *Mathematical and computer modelling* 2002; **36**(9-10):1131–1149.
15. Koçyigit MB, Falconer RA, Lin B. Three-dimensional numerical modelling of free surface flows with non-hydrostatic pressure. *International Journal for Numerical Methods in Fluids* 2002; **40**(9):1145–1162.
16. Yuan H, Wu CH. A two-dimensional vertical non-hydrostatic σ model with an implicit method for free-surface flows. *International Journal for Numerical Methods in Fluids* 2004; **44**(8):811–835.
17. Chen X. A fully hydrodynamic model for three-dimensional, free-surface flows. *International Journal for Numerical Methods in Fluids* 2003; **42**(9):929–952.
18. Zijlema M, Stelling GS. Further experiences with computing non-hydrostatic free-surface flows involving water waves. *International Journal for Numerical Methods in Fluids* 2005; **48**(2):169–197.
19. Fringer OB, Gerritsen M, Street RL. An unstructured-grid, finite-volume, nonhydrostatic, parallel coastal ocean simulator. *Ocean Modelling* 2006; **14**:139–173.
20. Badiei P, Namin MM, Ahmadi A. A three-dimensional non-hydrostatic vertical boundary fitted model for free-surface flows. *International Journal for Numerical Methods in Fluids* 2008; **56**(6):607–627.
21. Zhang Y, Baptista AM. Selfe: a semi-implicit eulerianŰlagrangian finite-element model for cross-scale ocean circulation. *Ocean Modelling* 2008; **21**(3–4):71–96.
22. Lai Z, Chen C, Cowles GW, Beardsley RC. A nonhydrostatic version of fvcom: 1. Validation experiments. *Journal of Geophysical Research* 2010; **115**(C11):C11010.
23. Bai Y, Cheung KF. Depth-integrated free-surface flow with a two-layer non-hydrostatic formulation. *International Journal for Numerical Methods in Fluids* 2012; **69**(2):411–429.

DOI: 10.1002/fld

24. Kleptsova O, Pietrzak JD, Stelling GS. On a momentum conservative z-layer unstructured c-grid ocean model with flooding. *Ocean Modelling* 2012; **54–55**(0):18–36.
25. Lesser GR, Roelvink JA, Van K, J, Stelling GS. Development and validation of a three-dimensional morphological model. *Coastal Engineering* 2004; **51**(8–9):883–915.
26. Peaceman DW, Rachford HH. The numerical solution of parabolic and elliptic differential equations. *Journal of the Society for Industrial and Applied Mathematics* 1955; **3**(1):28–41.
27. Griffies SM, Böning C, Bryan FO, Chassignet EP, Gerdes R, Hasumi H, Hirst A, Treguier AM, Webb D. Developments in ocean climate modelling. *Ocean Modelling* 2000; **2**(3-4):123–192.
28. Blumberg AF, Mellor GL. *A Description of a Three-dimensional Coastal Ocean Circulation Model, Three-dimensional Coastal Ocean Models, Ed. N. Heaps*. American Geophysical Union: Washington, DC, 1987. 1–16.
29. Shchepetkin AF, McWilliams JC. The regional oceanic modeling system: a split-explicit, free-surface, topography-following-coordinate ocean model. *Ocean Modelling* 2005; **9**:347–404.
30. Kanarska Y, Maderich V. A non-hydrostatic numerical model for calculating free-surface stratified flows. *Ocean Dynamics* 2003; **53**:176–185.
31. Kanarska Y, Shchepetkin A, McWilliams JC. Algorithm for non-hydrostatic dynamics in the regional oceanic modeling system. *Ocean Modelling* 2007; **18**(3–4):143–174.
32. Chorin AJ. Numerical solution of the navier-stokes equations. *Mathematics of Computation* 1968; **22**(104):745–762.
33. Harlow FH, Welch JE. Numerical Calculation of Time Dependent Viscous Incompressible Flow of Fluid with Free Surface. *Physics of Fluids* 1965; **8**(2182).
34. Bell JB, Colella P, Glaz HM. A second-order projection method for the incompressible Navier-Stokes equations. *Journal of Computational Physics* 1989; **85**(2):257–283.
35. Van Kan J. A second-order accurate pressure-correction scheme for viscous incompressible flow. *SIAM Journal on Scientific and Statistical Computing* 1986; **7**:870–891.
36. Armfield S, Street R. An analysis and comparison of the time accuracy of fractional-step methods for the Navier–Stokes equations on staggered grids. *International Journal for Numerical Methods in Fluids* 2002; **38**(3):255–282.
37. LeBlond PH, Mysak LA. *Waves in the Ocean*. Elsevier: Amsterdam, The Netherlands, 1978.
38. Kang D, Fringer OB. Time accuracy of pressure methods for nonhydrostatic free-surface flows. *Estuarine and Coastal Modeling 2005 – Proceedings of 9th International Conference on Estuarine and Coastal Modeling*, Charleston, South Carolina, 2005; 419–433. ASCE.
39. Gross ES, Bonaventura L, Rosatti G. Consistency with continuity in conservative advection schemes for free-surface models. *International Journal for Numerical Methods in Fluids* 2002; **38**:307–327.
40. Vitousek S, Fringer OB. Physical vs. numerical dispersion in nonhydrostatic ocean modeling. *Ocean Modelling* 2011; **40**(1):72–86.
41. Scotti A, Mitran S. An approximated method for the solution of elliptic problems in thin domains: application to nonlinear internal waves. *Ocean Modelling* 2008; **25**:144–153.
42. Leonard BP. A stable and accurate convective modelling procedure based on quadratic upstream interpolation. *Computer Methods in Applied Mechanics and Engineering* 1979; **19**:59–98.
43. Kim J, Moin P. Application of a fractional-step method to incompressible Navier-Stokes equations. *Journal of Computational Physics* 1985; **59**:308–323.
44. Zang Y, Street RL, Koseff JR. A non-staggered grid, fractional step method for time-dependent incompressible Navier-Stokes equations in curvilinear coordinates. *Journal of Computational Physics* 1994; **114**:18–33.

DOI: 10.1002/fld